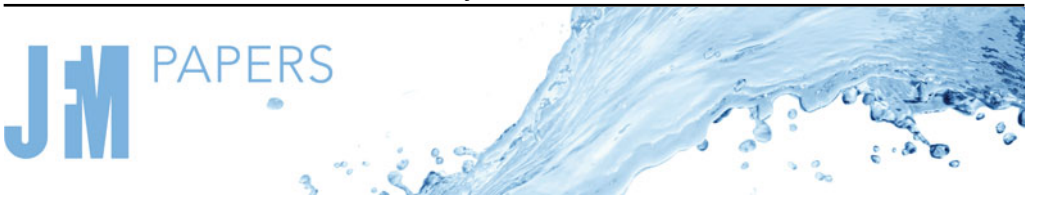
J. Fluid Mech. (2025), *vol.* 1016, A45, doi:10.1017/jfm.2025.10422



Investigation on the interaction between shoulder and tail cavities under vertical launching conditions

Zeyu Ren[1], **Xiaogang Wang**[1], **Xiaobo Quan**[2] **and Shaohua Cheng**[2]

[1]School of Astronautics, Harbin Institute of Technology, Harbin 150001, PR China

[2]Beijing Institute of Astronautical Systems Engineering, Beijing 100076, PR China

Corresponding author: Xiaogang Wang, wangxiaogang@hit.edu.cn

(Received 8 October 2024; revised 11 April 2025; accepted 20 June 2025)

This study investigates the fluid mechanisms underlying the interaction between ventilated shoulder and tail cavities under vertical launching conditions. It is found that expansion and contraction coexist within the tail cavity. When the expansion rate exceeds the contraction rate, the volume of the tail cavity increases; conversely, it decreases. Through this process, the cavity undergoes cyclic pulsation during its vertical evolution, including expansion, over-expansion, contraction and over-contraction. Before the shoulder cavity extends to the position of the tail cavity, wall confinement restricts the tail cavity from expanding towards the vehicle's lateral wall. After the encounter between the shoulder and tail cavities, the re-entrant flow at the end of the shoulder cavity induces the tail cavity to overcome wall confinement and expand towards the lateral wall, initiating their fusion. As a result, a supercavity forms and attaches to the surface of the vehicle. Moreover, after the fusion, the pressure driving mode at the vehicle's bottom wall shifts from the tail cavity pulsation to the re-entrant flow. In addition, an increase in the ventilation rate induces progressive expansion of the shoulder cavity's radial dimension, and accelerates its downstream propagation. The fusion mode between the shoulder and tail cavities transitions from progressive fusion to coverage fusion.

Key words: cavitation, multiphase flow, bubble dynamics

1. Introduction

During vertical launching, as shown in figure 1, an underwater vehicle progresses through three distinct phases: the launching stage, underwater navigation and water-exit, ultimately completing the entire trajectory (Zhang *et al.* 2005; Zhang, Yao & Zhang 2013; Wang & Huang 2018; Shi *et al.* 2022*b*). During the launching stage, the underwater vehicle is

© The Author(s), 2025. Published by Cambridge University Press.

https://doi.org/10.1017/jfm.2025.10422 Published online by Cambridge University Press

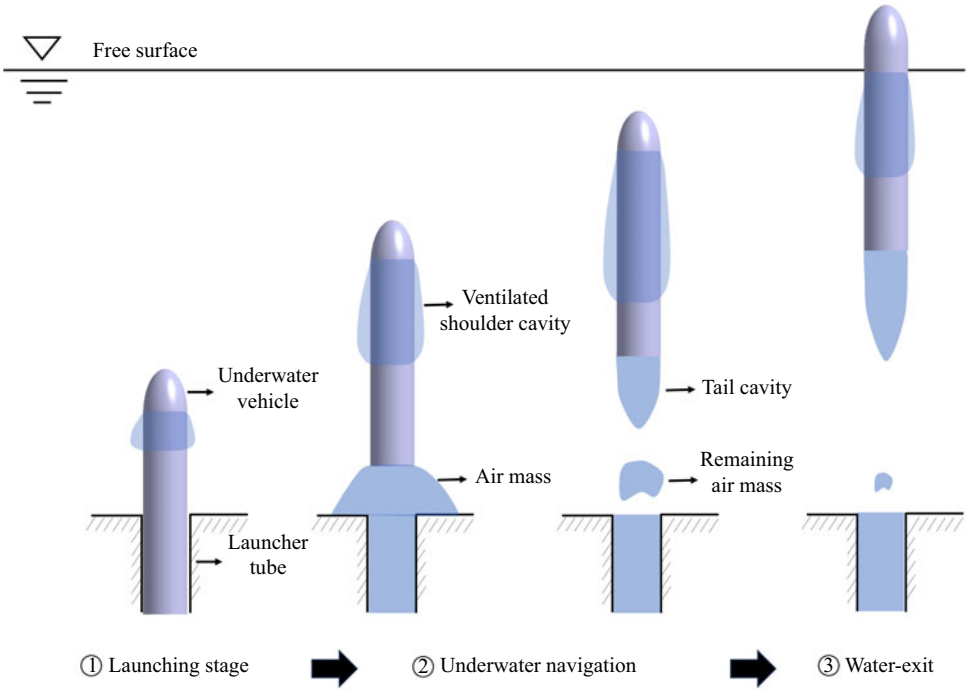


Figure 1. The process of underwater launching.

propelled by high-pressure gas towards the free surface, and finally exits the launcher tube. Subsequently, an air mass forms that bridges the vehicle's bottom wall and launcher tube exit. This air mass then ruptures, forming (i) a mobile tail cavity that adheres to the vehicle, and (ii) a remaining air mass that is stationary near the launcher tube exit (Zhou & Yu 2017; Cheng *et al.* 2022*b*; Yao *et al.* 2023). In addition, to maintain orientation stability, artificial ventilation is applied to generate ventilated shoulder cavities to fully envelop the underwater vehicle (Nguyen *et al.* 2022; Zhang, Lyu & Fan 2022). As a result, both tail and ventilated cavities simultaneously attach to the vehicle and interact dynamically, leading to cavity shedding, tail cavity rupture, and other unsteady effects that complicate the launching process (Chen *et al.* 2021*a*). Therefore, a thorough understanding of the coupled evolution of ventilated shoulder and tail cavities is essential for optimising the design of vertically moving underwater vehicles.

Initially, artificial ventilation was widely applied for horizontally moving vehicles. By blowing non-condensable gas into the low-pressure region at the shoulder, ventilated cavities can considerably reduce skin friction drag on underwater vehicles. When these cavities grow large enough to envelop most of the vehicle body, they enable high-speed movement (Epshtein 1973; Logvinovich 1973; Zhao *et al.* 2015; Sun *et al.* 2019). To date, water tunnels have served as an effective experimental platform for investigating ventilated cavitation. The platform enables systematic variation of flow conditions across a broad range of key parameters, including cavity pressure (P_C), ambient pressure (P_{atm}), incoming velocity (U), and ventilation flow rate (Q). These parameters commonly correspond to the following dimensionless groups: cavitation number $\sigma_c = (P_{atm} - P_C)/(0.5\rho U^2)$, air entrainment coefficient $C_Q = Q/UD^2$, Froude number $Fr = U/\sqrt{gD^2}$, where D , g and ρ denote feature size, gravitational acceleration and water density, respectively. In studies of ventilated cavities, gas leakage is an important

https://doi.org/10.1017/jfm.2025.10422 Published online by Cambridge University Press

phenomenon. Non-condensable gas escapes from the rear sealing region during the evolution of the ventilated cavity, resulting in multiple closure modes, such as re-entrant jet (Semenenko 2001; Kshatriya, Patwardhan & Eaglesham 2007), twin vortex (Spurk 2002), pulsating cavity (Skidmor 2013) and quad vortex (Kapankin & Gusev 1984; Kawakami & Arndt 2011). Subsequent researches have extensively investigated the underlying fluid mechanisms governing these closure modes. For example, Karn, Arndt & Hong (2016) confirmed that gravity served as a main factor in the generation of the twin vortices, resulting in vortex stretching and tilting processes. This caused the cavity to lift in the streamwise direction, creating a velocity difference between the upper and lower cavity surfaces, which led to subsequent flow separation. Moreover, through further experiments in a recirculating cavitation water tunnel at Saint Anthony Falls Laboratory, Karn *et al.* (2016), Shao *et al.* (2018) and Jiang, Shao & Hong (2018) have established connections among the dimensionless parameters governing the above-mentioned closure modes. To obtain detailed flow field characteristics, Wang *et al.* (2018) and Barbaca *et al.* (2019) utilised proper orthogonal decomposition methods to analyse coherent flow structures, including shear layers induced by Kelvin–Helmholtz instability. In addition, numerical studies, such as direct numerical simulations (Liu, Xiao & Shen 2023) and large-eddy simulations (LES) (Xiong *et al.* 2024), were also conducted to comprehend the flow mechanism of ventilated cavities.

Different from horizontally moving underwater vehicles, cavity evolution around a vertically moving underwater vehicle remains in a transient state with limited travel distance; the direction of gravity acts parallel to the vehicle's axial direction rather than radially. Without flow control, a natural cavity will adhere to the surface of the vehicle. During water-exit , the collapse of the natural cavity induces significant structural loading on the vehicle body, consequently compromising trajectory stability (Zhao *et al.* 2014; Wang *et al.* 2016; Fu *et al.* 2018; Gao *et al.* 2022*b*). Therefore, artificial ventilation is required to mitigate these adverse effects, enabling successful water-exit for underwater vehicles (Wang & Huang 2018). To generate ventilated cavities from the shoulder region to cover the vehicle surface, Zhang (2018), Hu (2018) and Gong (2018) jointly designed a ventilation system. Using this system, Chen *et al.* (2022) observed various closure modes for the ventilation cavities, including foamy cavity re-entrant jet twin vortex closure. However, the ventilated cavities obtained in their study, which featured large radial dimensions, were significantly affected by boundary conditions, resulting in extremely asymmetric cavity shape. To address this limitation, Qu *et al.* (2022) and Gan *et al.* (2022*a*,*b*) optimised both the experimental set-up and the underwater vehicle shape, investigating the effects of key parameters (e.g. Fr, C_Q and σ_c) on ventilated cavity evolution. They demonstrated that during water-exit, the non-condensable gas in ventilated cavities modified collapse behaviour and significantly reduced impact pressure compared to natural cavities. Considering the limited information obtained from experiments, Ma *et al.* (2018, 2019) and Gan *et al.* (2022*c*) employed the finite volume method to examine internal flow field structures within ventilated cavities. These investigations revealed various vortex structures, including shear-layer vortices and horseshoe vortices, which were found to significantly influence gas–liquid interface instability and subsequent flow pattern. Based on the potential flow theory, Li *et al.* (2019*a*,*b*, 2020) adopted the boundary element method to investigate three-dimensional ventilated cavity evolution under vertically incoming flow. Their results demonstrated that reduced surface tension significantly exacerbates cavity deformation. Ren *et al.* (2023) explored the impact of head shape on ventilated cloudy cavities, demonstrating that abrupt curvature variations in the head region attenuate inertial effects, thereby promoting the generation and detachment of cloudy ventilated cavities.

https://doi.org/10.1017/jfm.2025.10422 Published online by Cambridge University Press

As initially discussed, the vertical launching process is a complex procedure involving the coupling of ventilated and tail cavities. Early works for tail cavities were conducted by Zhang *et al.* (2017) and Xu *et al.* (2018) in the Harbin Institute of Technology HT01 Ventilation Cavity Water Tunnel. Similar works were later carried out by Cheng *et al.* (2022*a*), Yang *et al.* (2022*a*,*b*, 2023) and Quan & Cheng (2023). They installed a nozzle at the bottom of an underwater vehicle to eject supersonic or subsonic gas jets to generate ventilated tail cavities, and identified multiple types of cavities, including intact, foam, pulsating foam and broken cavities. To establish correlations among the dimensionless parameters governing the aforementioned tail cavity shapes, Xu *et al.* (2018) and Zhao *et al.* (2021) modified the traditional jet–cavity coupling model originally introduced by Paryshev (2006) and Kirschner *et al.* (2015). Their analysis revealed that the relative position between closure point of ventilated tail cavities and the iso-line of $P_0 = P_{0f}$ dominated tail cavity shapes, where P_0 and P_{0f} denoted the stagnation pressure and total incoming pressure, respectively. Considering vertically incoming flow, Qu *et al.* (2023) demonstrated the influence of surface tension coefficient S (expressed through the Weber number $We = \rho U^2 D/S$) on ventilated tail cavity morphology. Their results showed that a decrease in We intensified gas–liquid mixing at the cavity rear, and diminished air mass entrainment capacity, ultimately triggering foam cavity shedding. Extending this work, Yao *et al.* (2024) installed tail wings onto underwater vehicles to stabilise ventilated tail cavities, providing insights for deeper-water launch applications.

In vertical launching scenarios, a tail cavity forms as the vehicle leaves the air-filled launcher tube. The gas inside the tube, driven by inertia, follows the vehicle's upward motion and adheres to its bottom wall, thereby forming a tail cavity (see figure 1). Different from ventilated tail cavities, this type of cavity lacks a continuous gas supply after initial formation. Thus its morphology becomes difficult to maintain during subsequent transient evolution, leading to gas–liquid interface instability (Gao *et al.* 2022*c*,*d*). To investigate the hydrodynamic characteristics of tail cavities, Yao *et al.* (2023) designed a vertical launching experimental set-up featuring scaled model testing. Compared with the open water tank designed by Wang *et al.* (2012) and Sun, Sun & Zhao (2014), this set-up employed an air compressor to control ambient pressure P_{atm}, significantly mitigating scale effects. Experimental observations revealed distinct pulsation modes of the tail cavity during vertical launching: expansion, over-expansion, contraction and over-contraction. With an increase in cavity pulsation cycles, the cavity's gas entrainment capacity decreased progressively, leading to cavity shedding. Subsequently, a cooperative group of Yao *et al.* (2023) conducted a systematic investigation into the underlying fluid mechanisms governing these observed phenomena. Zhao *et al.* (2024) found that the cavitation number σ_c and tail cavity pulsation shared similar frequencies, only lagging by one phase. This also indicated that the pressure gradient across the cavity interface served as the primary driver of cavity pulsation. Ren *et al.* (2024) investigated the fluid mechanism governing cavity shedding, establishing a direct correlation between cavity shedding and vortex shedding. Their results demonstrated that U-shaped vortex and vortex ring shedding triggered foamy cavity shedding, whereas hairpin vortex shedding induced vortex tube shedding. It should be noted that these studies were limited to single launching, while practical engineering applications typically employ continuous launching to maximise operational efficiency. Lu *et al.* (2022*a*,*b*) experimentally investigated the impact of launch time interval on continuous launching. Their results demonstrated that an extended time interval significantly reduced the interference with the attitude of subsequently launched vehicles. However, constrained by experimental limitations, Lu *et al.* (2022*a*,*b*) were unable to explain the underlying fluid mechanisms. Numerical simulations performed by Gao *et al.* (2022*a*) and Shi *et al.* (2022*a*,*c*) revealed that hairpin

https://doi.org/10.1017/jfm.2025.10422 Published online by Cambridge University Press

vortices generated in the vehicle's wake region created a low-speed streak zone, leading to a reduction in both hydrodynamic force and pressure coefficients on subsequently launched vehicles. An increase in launch time interval significantly decreased the influence of the low-speed streak region, stabilising the attitude of subsequent vehicles.

Previous research primarily focused on tail cavities and ventilated cavities as separate phenomena (Gui *et al.* 2021; Sun *et al.* 2022). However, underwater vertical launching is a complex process coupling these two types of cavities. Thus based on our prior works (Ren *et al.* 2023, 2024, 2025), the current work presents detached-eddy simulations (DES) to investigate the cavity flow under vertical launching conditions, focusing on the interaction between the ventilated shoulder and tail cavities. This work is new and challenging. We aim to explore the underlying mechanisms of the interaction between the shoulder and tail cavities.

The remainder of this paper is organised as follows. Section 2 presents the numerical methods and parameter configurations employed in this study. Section 3 discusses the pulsation process of the tail cavity without considering the shoulder cavity. Section 4 subsequently investigates interactions between the tail and shoulder cavities, while § 5 examines how shoulder ventilation rates influence these interactions.

2. Methodology

This section presents the simulation set-up process. First, we introduce the division of the computational domain, followed by the grid generation strategy and the applied grid techniques. We conclude with the governing equations for numerical simulation.

2.1. *Computational domain*

To investigate the interaction between the shoulder and tail cavities, we employ a geometrically scaled underwater vehicle model (1 : 40) rather than a full-scale prototype. This ensures sufficient grid resolution for cavity simulation within feasible computational resources. As shown in figure 2(*a*), a complete three-dimensional computational domain is established. The computational domain for the underwater navigation phase is rectangular, with a reference frame established at the centre of the launcher tube exit. The computational domain spans $2L$ in the horizontal directions (x and y), and extends $5L$ in the vertical direction (z). The upper and outer boundaries are set as the pressure outlet conditions, and the bottom boundary is set as a wall condition. The computational domain of the launcher tube is shown in figure 2(*b*). The underwater vehicle, with a cylindrical geometric shape and an elliptical nose, is assumed to move at a constant speed opposite to the gravity direction. The vehicle's slenderness ratio is 6 : 1 (length $L = 330$ mm, diameter $D = 55$ mm). The air seam, serving as a mass flow inlet for non-condensable gas discharge to generate a ventilated shoulder cavity, is installed at the vehicle's shoulder zone. The launcher tube is cylindrical, with diameter D and length $1.5L$. The tube's lateral wall is set as a wall boundary condition. As the vehicle passes through the launcher tube, constant internal pressure is maintained via a pressure outlet condition at the tube bottom. Upon exiting the tube, the boundary condition transitions to a wall condition, terminating gas supply.

In the current work, several dimensionless parameters are defined to determine the initial conditions and for subsequent data analysis.

The Froude number Fr is

$$Fr = \frac{u_v}{\sqrt{gL}}, \tag{2.1}$$

where Fr is employed to determine the velocity of the vehicle u_v.

https://doi.org/10.1017/jfm.2025.10422 Published online by Cambridge University Press

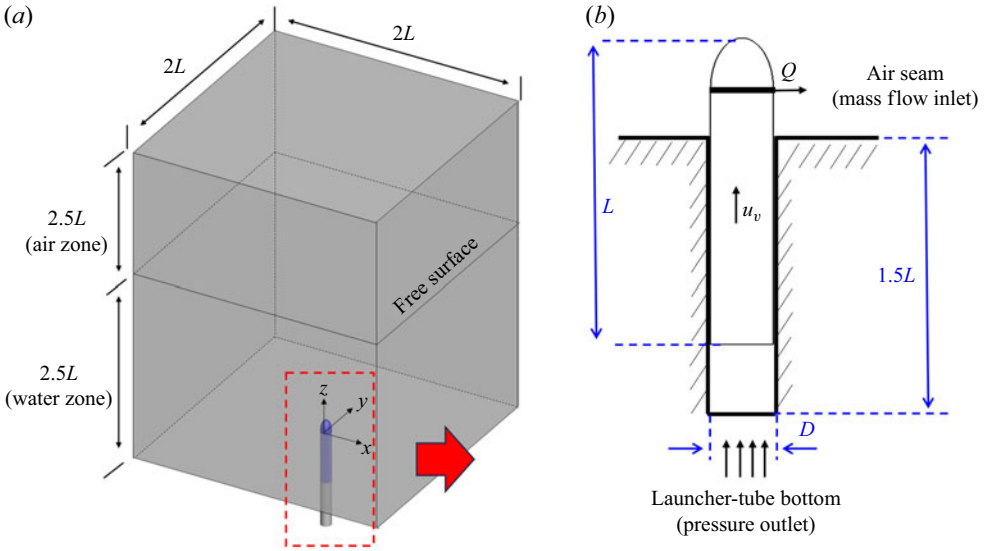


Figure 2. Division of computational domains. (*a*) Rectangular computational domain, where L and D represent the length and width of the vehicle, respectively, u_v is the velocity of the vehicle, and Q is the ventilation rate. (*b*) Computational domain of the launcher tube.

The cavitation number σ is

$$\sigma = \frac{P_{atm} - P_v}{0.5\rho_w U^2}, \tag{2.2}$$

where P_v is the saturated vapour pressure of water. Here, σ is used to determine the atmospheric pressure P_{atm}.

The dimensionless launching pressure P_r is

$$P_r = \frac{P_{in}}{P_{atm} + \rho g H_0}, \tag{2.3}$$

where P_r is used to determine the initial pressure of the launcher (P_{in}) during the launching stage.

The dimensionless ventilation flow rate $\bar{Q}$ is

$$\bar{Q} = \frac{Q}{u_v L^2}, \tag{2.4}$$

where Q is the ventilation flow rate on the air seam.

The dimensionless displacement of vehicle movement $\bar{H}$ is

$$\bar{H} = \frac{H}{L}, \tag{2.5}$$

where H is the vertical location of the vehicle's bottom wall.

The dimensionless pressure $\bar{P}$ is

$$\bar{P} = \frac{P - [P_{atm} + \rho g(H_0 - H)]}{P_{atm} + \rho g H_0}, \tag{2.6}$$

where P is the pressure of the fluid field.

https://doi.org/10.1017/jfm.2025.10422 Published online by Cambridge University Press

Case	Fr	σ	P_r	$\bar{Q}$
1	2.22	0.29	1.25	0
2	2.22	0.29	1.25	7.12×10^{-4}
3	2.22	0.29	1.25	3.56×10^{-3}
4	2.22	0.29	1.25	1.10×10^{-2}

Table 1. Initial conditions of each case in the present numerical simulations.

The average dimensionless pressure at the bottom wall of the vehicle $\bar{P}_B$ is

$$\bar{P}_B = \frac{P_B - [P_{atm} + \rho g(H_0 - H_B)]}{P_{atm} + \rho g h_0}, \tag{2.7}$$

where H_B is the vertical location of the vehicle's bottom wall.

Based on geometric scaling, Fr is the primary dynamic similarity law, which results in a velocity scaling relationship $u_{vm} = \sqrt{\lambda}\, u_{vp}$, where λ is the scale ratio $1/40$, and u_{vm} and u_{vp} denote the velocities of the model and prototype vehicles, respectively. The similarity of σ yields a pressure scaling $P_{atmm} - P_v = \lambda(P_{atmp} - P_v)$, where P_{atmm} and P_{atmp} are atmospheric pressures of the model and prototype vehicles, respectively. The dynamic similarity laws are developed based on works of Chen *et al.* (2021*b*) and Ma *et al.* (2023), and are aconsistent with our previous studies (Ren *et al.* 2023, 2024). In fact, scaled-down simulation is also adopted as a practical approach to obtain more detailed flow field information under the constraints of limited computational resources. Moreover, P_r is used to characterise the initial pressure inside the launcher tube during the launching stage. Here, $\bar{H}$, $\bar{P}$ and $\bar{P}_B$ are employed for quantitative analysis. Table 1 summarises the initial conditions of numerical cases presented in this paper.

2.2. *Grid division and technique*

To prevent gas leakage during the launching stage, which can affect the evolution of cavities, the diameter of the launcher tube is set equal to that of the underwater vehicle in this simulation. Therefore, a zero-gap overlapping grid technique (Shi *et al.* 2022*a*) is applied to address the treatment of overlapping wall boundary conditions. The technique deactivates the wall boundary grid and establishes a temporary interface between the corresponding regions, thereby ensuring the stability of the numerical simulation during the launching stage. Figure 3 illustrates the grid division strategy. The mesh height for the first layer is 5.0×10^{-7}m at the vehicle boundary, and 5.0×10^{-6}m at the launcher tube boundary, with corresponding growth rates 1.1 and 1.2. The average grid size Δ_{avg} in the vehicle's movement region is 1.5 mm, and the time step is set as $\Delta_{avg}/(10U)$. Grid independence verification and mesh details are provided in Appendix A.

To provide sufficient resolution of the gas–liquid interface and accurately capture the unsteady evolution of cavities, adaptive mesh refinement (AMR) technology is employed. As shown in figure 4, the grid is refined by two levels in regions where the volume fraction of water α ranges between 0.2 and 0.8, and the vertical position z is between $0L$ and $2.5L$. In addition, the octree method is adopted for grid refinement, and data interpolation is performed for data transfer between the coarse and fine grids.

2.3. *Numerical methods*

Based on the finite volume method, the interaction between shoulder and tail cavities is simulated using the commercial computational fluid dynamics software STAR-CCM+.

https://doi.org/10.1017/jfm.2025.10422 Published online by Cambridge University Press

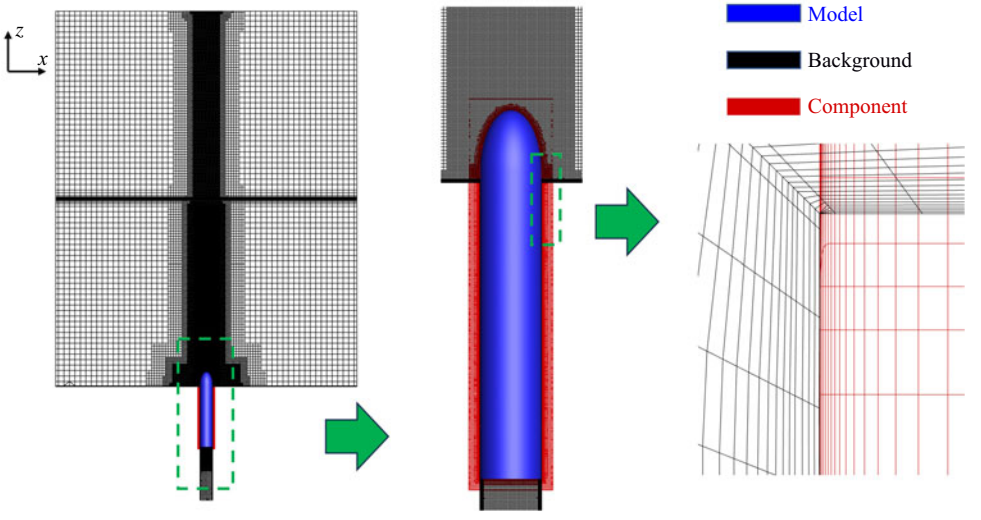


Figure 3. Grid division. The grids in the background and overlapping regions are represented in black and red, respectively. The geometric model is shown in blue.

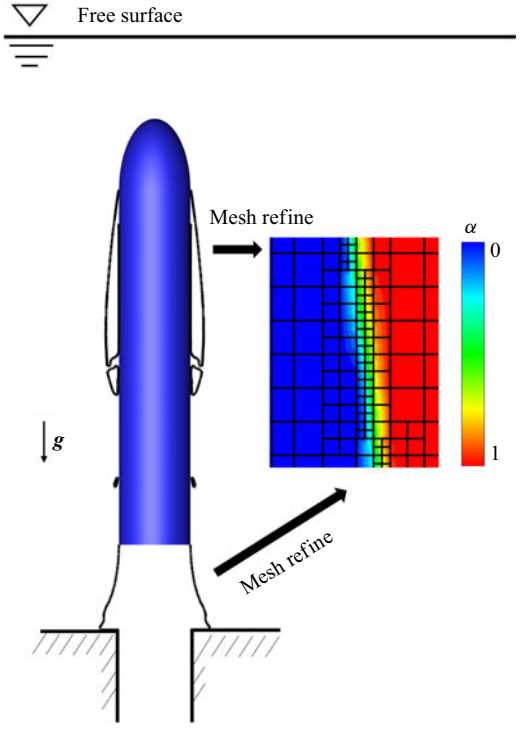


Figure 4. Strategy of AMR. The simulation result is obtained from case 1 at $\bar{H} = 0.20$, where $\bar{H}$ is the dimensionless vertical position of the vehicle's bottom wall. The iso-line of 90 % water volume fraction is used to illustrate the tail cavity shape.

https://doi.org/10.1017/jfm.2025.10422 Published online by Cambridge University Press

The fluid field is modelled as a two-phase flow (water and gas), with natural cavitation effects neglected. Air is modelled as a compressible ideal gas, while water is treated as an incompressible fluid. The air phase follows the ideal gas law $P = \rho RT$, where P is the pressure, ρ is the air density, R is the gas constant with value 287 J kg^{-1} K^{-1}, and T is the absolute temperature. The specific heat ratio is defined as $\gamma = C_P/C_v$, where C_P is the specific heat at constant pressure with value 1005 J kg^{-1} K^{-1}, and C_v is the specific heat at constant volume. The volume of fluid method (Hirt & Nichols 1981) is employed for the multiphase flow calculation, with a high-resolution interface capture scheme for discretising the convective flux in the volume of fluid transport equation (Gao *et al.* 2022*c*). The DES method (Spalart *et al.* 2006) is used for the turbulence calculation. Using DES is a hybrid turbulence modelling approach that combines Reynolds-averaged Navier–Stokes (RANS) simulations and LES. The governing equations are introduced below.

The volume fraction equation is

$$\frac{\partial \alpha_k}{\partial t} + \nabla \cdot (\alpha_k \boldsymbol{u}) = 0. \tag{2.8}$$

The continuity equation is

$$\frac{\partial \rho_m}{\partial t} + \nabla \cdot (\rho_m \boldsymbol{u}) = 0. \tag{2.9}$$

The momentum equation of RANS simulations is

$$\frac{\partial \rho_m \boldsymbol{u}}{\partial t} + \nabla \cdot (\rho_m \boldsymbol{u} \otimes \boldsymbol{u}) = -\nabla \cdot p\boldsymbol{I} + \nabla \cdot \left(\bar{\boldsymbol{T}} + \boldsymbol{T}_{RANS}\right) + \boldsymbol{F}. \tag{2.10}$$

The momentum equation of LES is

$$\frac{\partial \rho_m \tilde{\boldsymbol{u}}}{\partial t} + \nabla \cdot (\rho_m \tilde{\boldsymbol{u}} \otimes \tilde{\boldsymbol{u}}) = -\nabla \cdot \tilde{p}\boldsymbol{I} + \nabla \cdot \left(\tilde{\boldsymbol{T}} + \boldsymbol{T}_{SGS}\right) + \boldsymbol{F}, \tag{2.11}$$

where α_k denotes the volume fraction of each phase, ρ_m is the mixture density of fluid, $\boldsymbol{u}$ is the RANS velocity, $\tilde{\boldsymbol{u}}$ is the LES filtered velocity, $\tilde{p}$ is the filtered pressure, $\boldsymbol{T}$ is the mean viscous stress tensor, $\tilde{\boldsymbol{T}}$ is the filtered stress tensor, $\boldsymbol{T}_{RANS}$ is the Reynolds-stress tensor, $\boldsymbol{T}_{SGS}$ is subgrid-scale stress tensor, and $\boldsymbol{F}$ is the body force term.

The present simulation employs the shear stress transport (SST) k-ω model (Menter 1994) for RANS simulations, which is a two-equation model that considers the transport of turbulence shear stress and introduces the blending function. The governing equations of the SST k-ω model are

$$\frac{\partial \rho_m k}{\partial t} + \nabla \cdot (\rho_m k \boldsymbol{u}) = \nabla \cdot [(\mu_m + \sigma_k \mu_t)\, \nabla k] - f_{\beta^*} \beta^* \rho_m \tilde{\omega} k + P_k, \tag{2.12}$$

$$\frac{\partial \rho_m \omega}{\partial t} + \nabla \cdot (\rho_m \omega \boldsymbol{u}) = \nabla \cdot [(\mu_m + \sigma_\omega \mu_t)\, \nabla \omega] - f_\beta \beta \rho_m \omega^2 + P_\omega, \tag{2.13}$$

where k is the turbulent kinetic energy, μ_m is the dynamic viscosity of the mixture, μ_t is the turbulent viscosity, ω is the turbulent frequency, σ_k and σ_Ω denote the turbulent model constants, f_β is the vortex-stretching modification factor, f_{β^*} is the shear modification factor, β and β^* are model coefficients, and P_k and P_ω are production terms. Notably, ω is modified to address the problem of modelled stress depletion (Spalart *et al.* 2006; Shur *et al.* 2008), which can occur when the separation region is narrow or the boundary layer is thick. In the current simulation, the semi-implicit method for pressure-linked equations (SIMPLE) is used to solve the pressure–velocity coupling in the flow field. Both time and spatial terms are discretised using a second-order upwind scheme. In addition, the surface

https://doi.org/10.1017/jfm.2025.10422 Published online by Cambridge University Press

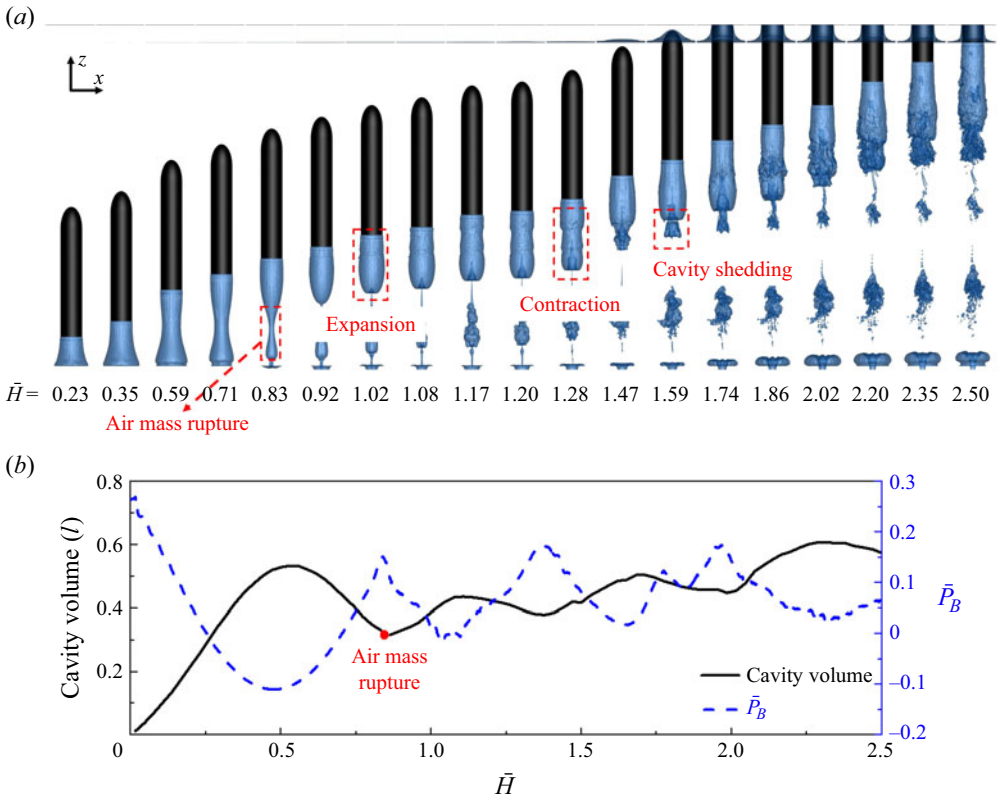


Figure 5. The evolution process of tail cavities without shoulder cavities attached. (*a*) The flow patterns of tail cavities. The iso-surface of 90 % water volume fraction is used to illustrate the tail cavity shape. (*b*) The variation of cavity volume and $\bar{P}_B$ with $\bar{H}$.

tension model is employed (Xiong *et al.* 2024), and the surface tension coefficient is taken as 0.072 N m^{-1}.

3. The evolution of tail cavities without shoulder cavities attached

In this section, simulation results for case 1 are presented to investigate the flow characteristics of tail cavity pulsation in the absence of shoulder cavities. The flow patterns of tail cavities are shown in figure 5(*a*). At $\bar{H} = 0.23-0.71$, the underwater vehicle initially leaves the launcher tube while remaining connected to it by an air mass. As the vehicle moves towards the free surface, the air mass undergoes necking and eventually ruptures, forming a tail cavity attached to the vehicle's bottom wall. Subsequently, the tail cavity initiates its unsteady evolution process. Regarding flow patterns, the tail cavity undergoes periodic expansion and contraction. During transitional phases between pulsation cycles (specifically during contraction-to-expansion transitions), large-scale cavity shedding occurs at the tail cavity's rear portion (as marked in figure 5*a*). The variation of cavity volume and $\bar{P}_B$ with $\bar{H}$ is provide in figure 5(*b*). At $\bar{H} = 0.00-0.74$, the underwater vehicle remains connected to the launcher tube via an air mass. Initially, the air mass internal pressure significantly exceeds the ambient pressure, driving rapid cavity volume expansion. As internal pressure progressively decreases below ambient pressure, the cavity volume contracts, leading to the air mass rupture, evidenced by a distinct discontinuity

https://doi.org/10.1017/jfm.2025.10422 Published online by Cambridge University Press

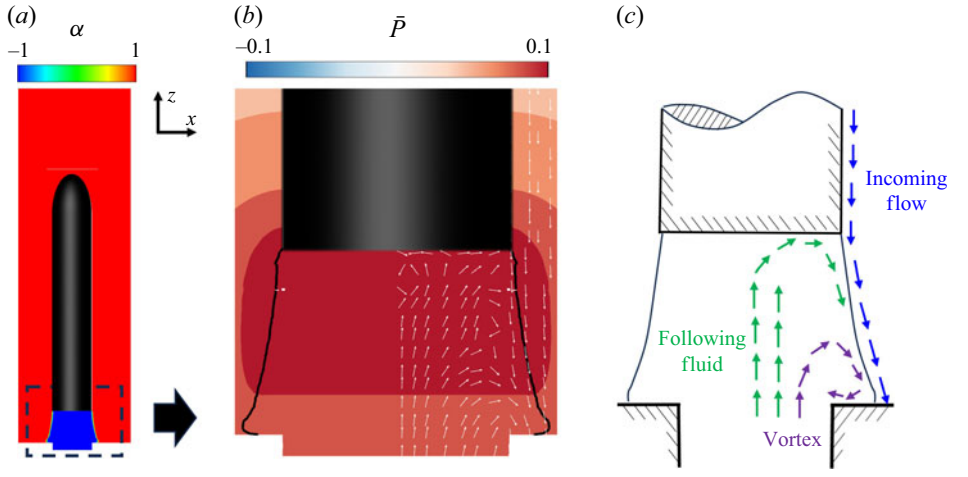


Figure 6. The expansion of the air mass at $\bar{H} = 0.14$. (*a*) The flow pattern of the air mass. (*b*) The contour of dimensionless pressure $\bar{P}$. The iso-line of 90 % water volume fraction is used to illustrate the air mass shape. The velocity field is in reference to the underwater vehicle. (*c*) Scheme of fluid particle motion.

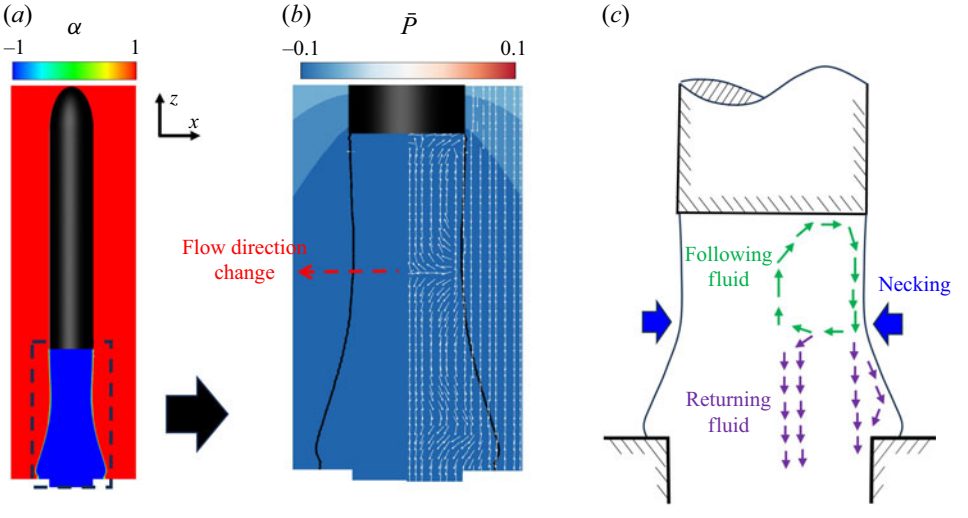


Figure 7. The contraction of the air mass at $\bar{H} = 0.50$. (*a*) The flow pattern of the air mass. (*b*) The contour of dimensionless pressure $\bar{P}$. The iso-line of 90 % water volume fraction is used to illustrate the air mass shape. The velocity field is in reference to the underwater vehicle. (*c*) Scheme of fluid particle motion.

in the cavity volume curve at $\bar{H} = 0.74$. Following this rupture, a tail cavity forms and attaches to the bottom wall of the vertically moving vehicle. Pressure differences between the interior and exterior of the tail cavity drive periodic cavity pulsations, characterised by continuous expansion–contraction cycles. In addition, throughout the entire underwater navigation process, the volume of the tail cavity continues to increase due to the ambient pressure reduction caused by vertical movement.

Figures 6 and 7 illustrate the detailed flow field during air mass necking, where a positive value of the dimensionless pressure $\bar{P}$ indicates that the internal air mass pressure exceeds the ambient pressure, whereas a negative value indicates the inverse relationship. In figure 6, the pressure inside the air mass substantially exceeds ambient pressure, resulting in an expansion trend of the air mass . At this position, the underwater vehicle leaves

https://doi.org/10.1017/jfm.2025.10422 Published online by Cambridge University Press

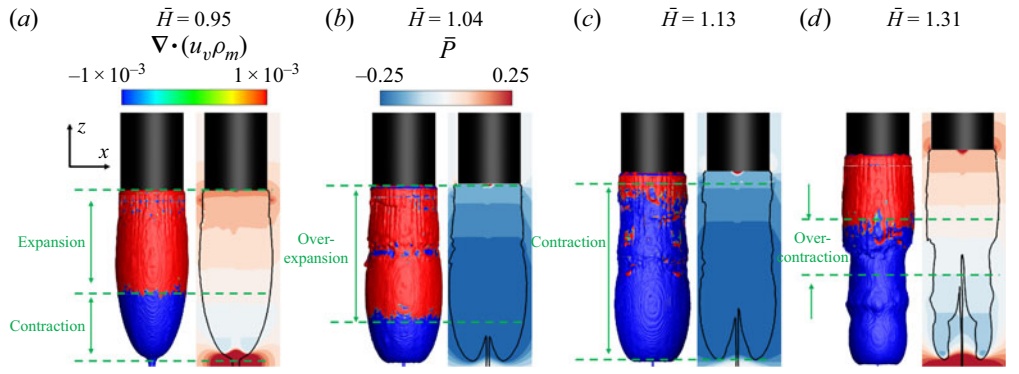


Figure 8. The pulsation process of the tail cavity, where $\nabla\cdot(\boldsymbol{V}\rho_m)$ represents the mass flux. A positive value of $\nabla\cdot(\boldsymbol{V}\rho_m)$ indicates expansion of the cavity shape, whereas a negative value indicates contraction. In addition, the iso-line of 90% water volume fraction is used to illustrate the tail cavity shape.

the launcher tube with a constant speed, and drives the internal gas to move along with it. However, constrained by the incoming flow with high kinetic energy, the flow direction deflects upon impinging on the vehicle's bottom wall, and subsequently turns downstream. In comparison, the fluid near the tube exit imposes weaker constraints on the air mass, making it the primary region of expansion. Additionally, due to the abrupt change in curvature, a large-scale vortex forms at the tube exit. As the air mass continues to expand, its internal pressure gradually drops below the ambient pressure, thereby initiating the contraction process. As shown in figure 7, the moving vehicle is capable of carrying only a limited amount of trailing fluid. As the air mass begins to contract, the residual fluid within it, defined as the returning flow, starts to move downstream and re-enters the launcher tube. The most pronounced necking of the air mass during contraction occurs at the location where the flow direction changes, as this region offers the weakest resistance to contraction. As the necking progresses, the air mass eventually ruptures, leading to the formation of a tail cavity.

To investigate the pulsation mechanism of the tail cavity, $\nabla\cdot(\boldsymbol{u}\rho_m)$ is applied to quantitatively characterise the expansion and contraction processes. A positive value of $\nabla\cdot(\boldsymbol{u}\rho_m)$ indicates cavity expansion, whereas a negative value indicates contraction. As shown in figure 8, expansion and contraction coexist within the tail cavity. This is a distinct phenomenon, differing from the typical pulsation behaviour of bubbles in a free flow field (Zhang *et al.* 2023). On the one hand, under vertical launching conditions, the tail cavity exhibits a large size in the direction of gravity, resulting in significant variations in ambient pressure along its length. On the other hand, as displacement gradually increases, water pressure continuously decreases. These factors cause the transitions between cavity expansion and contraction to consistently occur in the upstream region of the tail cavity. Meanwhile, in the downstream region, the cavity remains in a state of contraction due to greater water depth. In figure 8, at $\bar{H} = 0.95$, the internal pressure of the upstream cavity exceeds the ambient pressure, causing expansion. At $\bar{H} = 1.04$, as the cavity volume increases, the internal pressure gradually drops below the ambient pressure. However, the marked cavity region in figure 8(*b*) continues to expand due to inertia effects, a phenomenon referred to as over-expansion. At $\bar{H} = 1.13$ and 1.31, the tail cavity undergoes sequential contraction and over-contraction. This indicates that the change in cavity volume is a relative process. When the rate of expansion exceeds the contraction, the volume of the tail cavity increases; conversely, the cavity volume decreases. Based on the characteristics of volume variation, figures 8(*a*), 8(*b*), 8(*c*) and 8(*d*) are defined as

https://doi.org/10.1017/jfm.2025.10422 Published online by Cambridge University Press

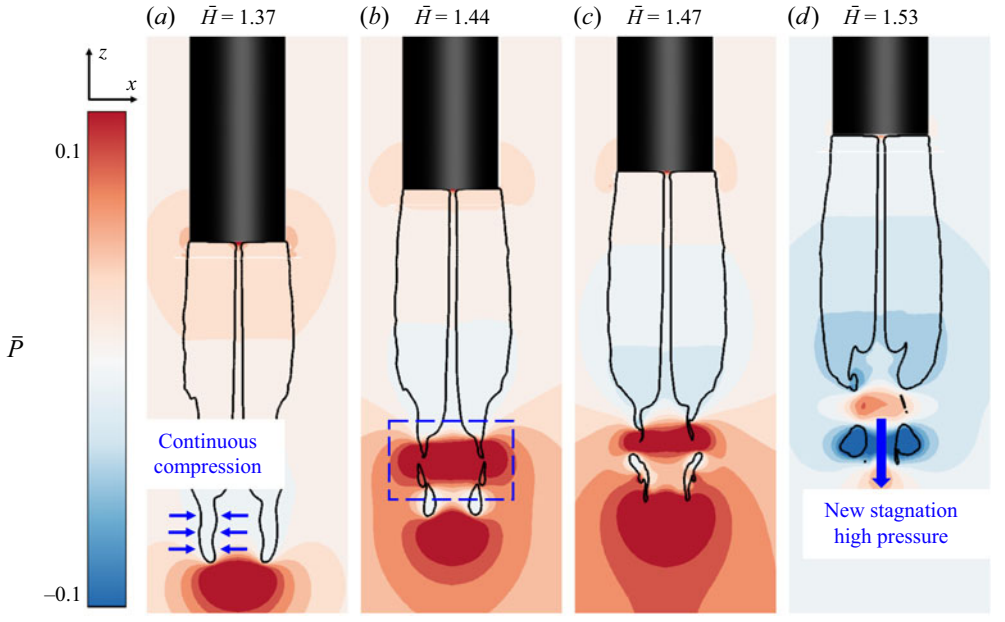


Figure 9. The process of cavity shedding. The iso-line of 90 % water volume fraction is used to illustrate the tail cavity shape.

expansion, over-expansion, contraction and over-contraction, respectively, which together constitute a complete pulsation cycle. In addition, due to over-expansion and over-contraction, the change of cavity volume usually lags behind the change of pressure. As the tail cavity pulsation repeats, cavity shedding occurs. As shown in figure 9, at $\bar{H} = 1.73$, the rear of the tail cavity undergoes continuous compression due to the combined effects of ambient pressure and stagnation high pressure. Ultimately, the tail cavity is cut off, leading to cavity shedding and the generation of significant shear stress, as marked in figure 9(*b*). In addition, a new stagnation high-pressure point forms at the location where cavity shedding occurs.

Through the above mechanistic analysis, a more precise understanding of the tail cavity pulsation process is obtained. However, when considering the presence of the shoulder cavity, particularly when it extends to the region of the tail cavity, how do the two cavities interact? This issue is discussed in the next section of this study.

4. The analysis of the interaction between ventilated and tail cavities

In this section, case 2 is set as a typical working condition to analyse the interaction between shoulder and tail cavities. The cavity flow patterns during the underwater navigation stage are exhibited in figure 10. Before the underwater vehicle exits the launcher tube, non-condensable gas is expelled through the air seam to form the shoulder cavity. However, owing to the buoyancy effect and the high momentum of the non-condensable gas, the initial radial size of the shoulder cavity is relatively large at $\bar{H} = -0.46$. Subsequently, flow separation at the end of the shoulder cavity causes this portion of the cavity to gradually contract and eventually shed at $\bar{H} = 0.08$. The detached cavity moves downstream and interacts with the air mass near the launcher tube exit, leading to earlier rupture and greater instability of the gas–liquid interface compared to conditions without shoulder cavity attachment (case 1). At $\bar{H} = 0.62$, the shoulder and tail cavities encounter

https://doi.org/10.1017/jfm.2025.10422 Published online by Cambridge University Press

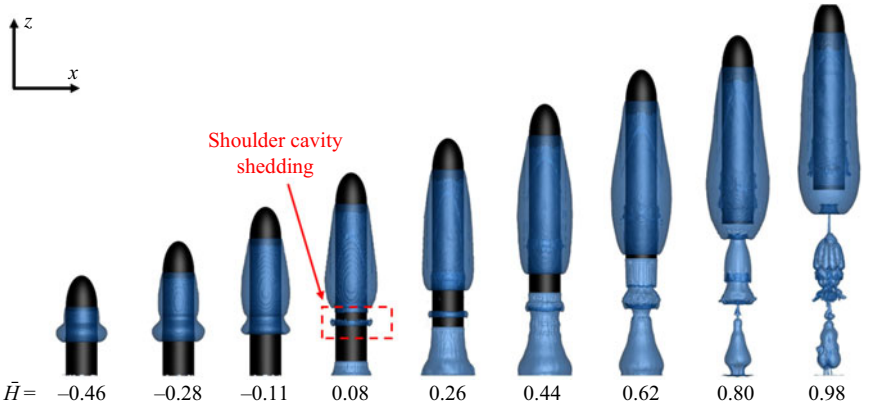


Figure 10. The cavity evolution in case 2. The iso-surface of 90 % water volume fraction is used to illustrate the tail cavity shape.

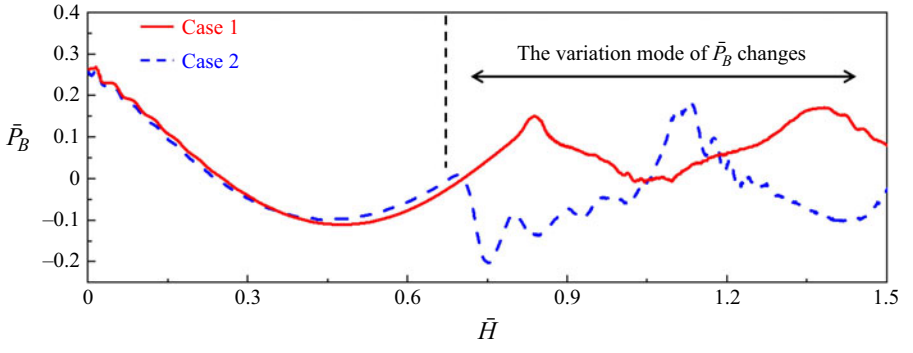


Figure 11. The variation of $\bar{P}_B$ with $\bar{H}$ under the comparison of cases 1 and 2. Case 1 takes into account the attachment of the shoulder cavity, whereas case 2 does not.

the bottom wall of the underwater vehicle. Subsequently, the shoulder and tail cavities merge, forming a supercavity attached to the vehicle surface.

Additionally, the variation modes of pressure at the bottom wall are critical to the success of underwater launches, and represent one of the primary focuses of this study. Figure 11 shows the variation of $\bar{P}_B$ with $\bar{H}$ for cases 1 and 2. Before $\bar{H} = 0.67$, the variation modes of $\bar{P}_B$ in the two cases are similar. However, after this point, the variation modes of $\bar{P}_B$ diverge completely. As described in § 3, in case 1, the pressure pulsation is driven primarily by the contraction and expansion of the tail cavity, without the attachment of a shoulder cavity. When the shoulder cavity is taken into consideration (case 2), the frequency of pressure pulsation increases significantly. However, the underlying fluid mechanics of this phenomenon remain unclear.

In the following subsections, this interaction process is decomposed into various stages, with different analytical methods employed.

4.1. *The fusion process of the shoulder and tail cavities*

Figure 12 shows the details of the flow field at $\bar{H} = 0.68$ in case 2. At this location, although the re-entrant jet at the end of the shoulder cavity causes fluid particles to move upstream, the distance between the shoulder and tail cavities is too large for the re-entrant

https://doi.org/10.1017/jfm.2025.10422 Published online by Cambridge University Press

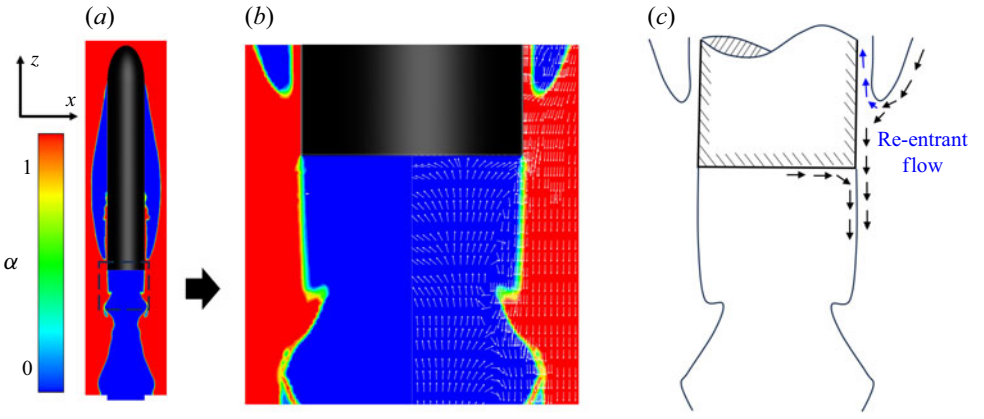


Figure 12. Details of the flow field at $\bar{H} = 0.56$ in case 2. (*a*) The flow pattern of the cavity. (*b*) The flow field of the marked region. The iso-line of 90 % water volume fraction is used to illustrate the cavity shape. (*c*) Scheme of fluid particle motion.

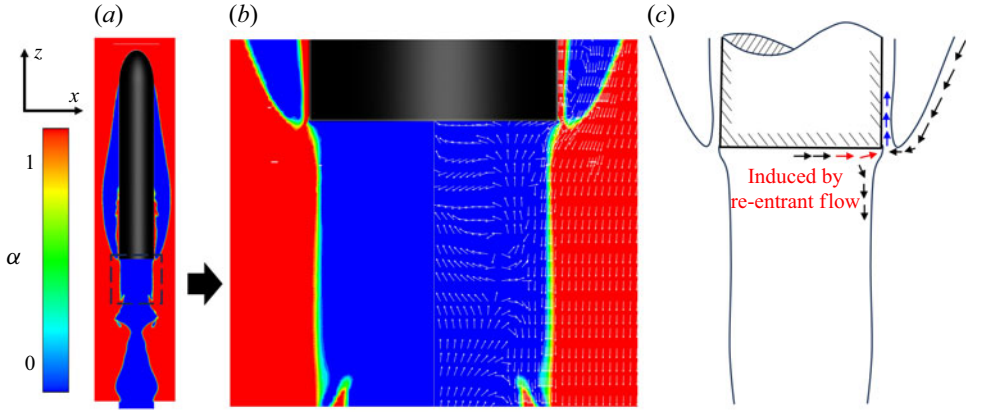


Figure 13. Details of the flow field at $\bar{H} = 0.68$ in case 2. (*a*) The flow pattern of the cavity. (*b*) The flow field of the marked region. The iso-line of 90 % water volume fraction is used to illustrate the cavity shape. (*c*) Scheme of fluid particle motion.

jet to influence the flow pattern of the tail cavity. Consequently, the tail cavity remains unable to break through the confinement and expand towards the lateral wall. As the shoulder cavity continues to propagate, it approaches and interacts with the tail cavity. As shown in figure 13, the re-entrant jet from the shoulder cavity induces fluid particles near the tail cavity boundary to move towards the vehicle's lateral wall, thereby initiating the fusion process between the shoulder and tail cavities.

Subsequently, the tail cavity continues to develop upstream, while the shoulder cavity progresses downstream, ultimately leading to their encounter. However, as shown in figure 14, due to the influence of surface tension, the two cavity boundaries do not fully merge but instead form a boundary resembling a liquid film, referred to as the fusion line (FL). Affected by the FL, the upstream motion of the fluid particles is impeded, leading to the formation of a large-scale vortex in front of the FL (at $\bar{H} = 0.7015$). At the same time, the tail cavity drives the FL to continue moving upstream. During the process, part of the FL disappears, and the two regions gradually merge. Some fluid particles from the tail cavity converge into the vortex in front of the FL, while others continue to move upstream

https://doi.org/10.1017/jfm.2025.10422 Published online by Cambridge University Press

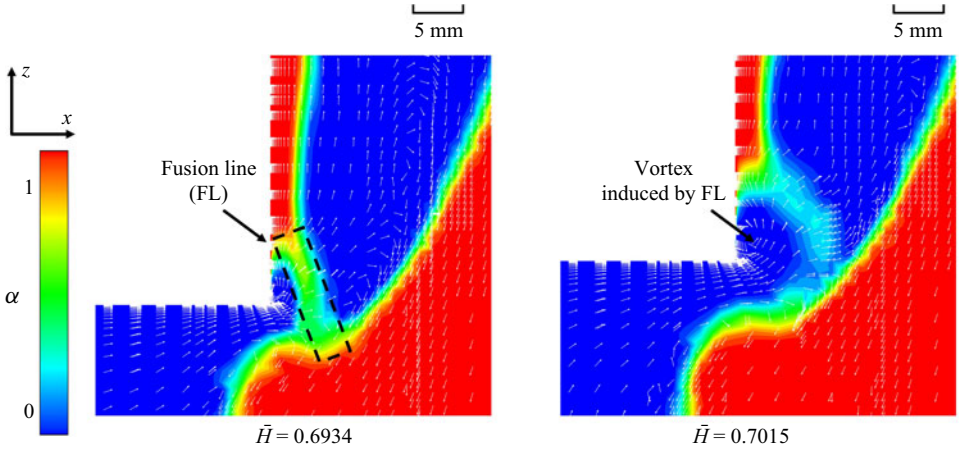


Figure 14. Fusion process of the shoulder and tail cavities in case 2.

towards the shoulder cavity. Eventually, the two cavities completely merge, and the FL disappears.

4.2. *The impact of shoulder cavity on the flow pattern of the tail cavity*

As previously exhibited in figure 10 ($\bar{H} = 0.14-1.11$), the influence of the shoulder cavity on the evolution of the tail cavity can be divided primarily into two stages: before and after the shoulder cavity extends to the location of the tail cavity.

Before this, under the combined effects of buoyancy and incoming flow, a small portion of the cavity detaches from the shoulder cavity and moves downstream along the vehicle (Ren *et al.* 2021). As this shedding cavity encounters the tail cavity, it intensifies the instability of the gas–liquid interface of the tail cavity (as shown in figure 15*b*). By comparing figure 15(*a*), which represents the condition without the shoulder cavity attached (case 1), it is found that the shedding cavity accelerated the velocity of the surrounding fluid, thereby increasing the contraction rate of the downstream cavity. At the same time, the contraction rate of the upstream cavity significantly decreases. The significant difference in the contraction rates along the gas–liquid interface causes the instability on the interface.

After that, the tail cavity is gradually cut off by the shoulder cavity (as exhibited in figure 10 at $\bar{H} = 0.80$). Figure 16 presents the detailed process. At $\bar{H} = 0.71$, upon the encounter of the shoulder and tail cavities, the motion of fluid particles diverges into two directions: one portion flows upstream towards the shoulder cavity, while the other merges into the downstream region, forming a small-scale vortex and leading to a reduction in the radial dimension of the tail cavity. At $\bar{H} = 0.74$, as the cavity develops, the vortex size gradually increases, continuously compressing the radial dimension of the tail cavity, and ultimately leading to its rupture and the formation of the supercavity.

In order to quantitatively analyse the velocity field, the dimensionless relative velocity $\bar{u}_{ref}$ and height $\bar{H}_{ref}$ are defined as

$$\bar{u}_{ref} = \frac{u_{ref}}{\sqrt{gl}}, \tag{4.1}$$

$$\bar{H}_{ref} = \frac{H_c - H}{L}, \tag{4.2}$$

https://doi.org/10.1017/jfm.2025.10422 Published online by Cambridge University Press

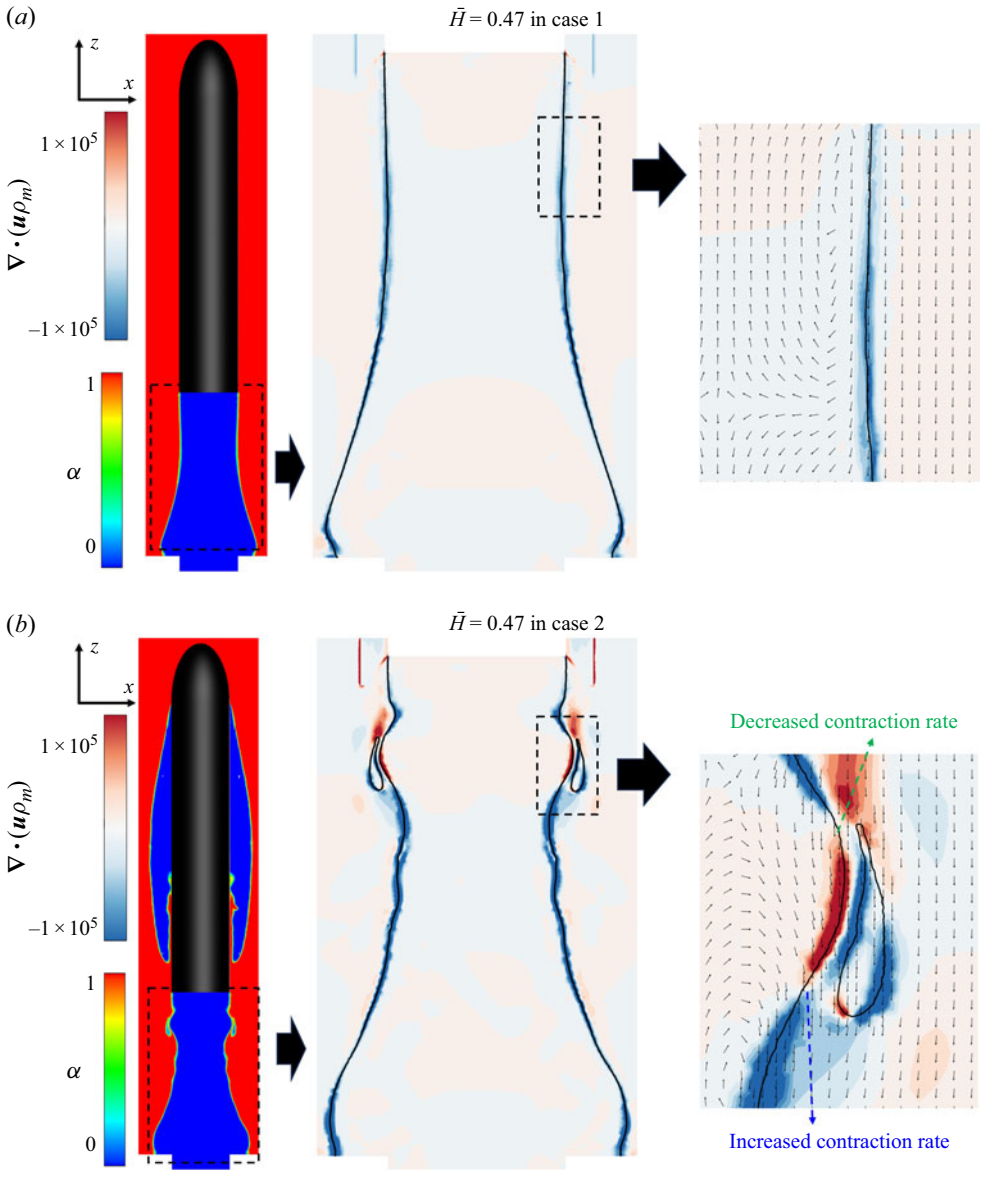


Figure 15. The impact of the shedding cavity on the tail cavity evolution, where $\nabla \cdot (\boldsymbol{u}\rho_m)$ represents the mass flux. A positive value of $\nabla \cdot (\boldsymbol{u}\rho_m)$ indicates an expansion of the cavity shape, whereas a negative value indicates contraction. In addition, the iso-line of 90 % water volume fraction is used to illustrate the cavity shape.

where u_{ref} is the velocity of the flow field relative to the vehicle, and H_c is the vertical position of the origin (as marked on the right-hand side of figure 17*a*). As shown in figures 17(*a*) and 17(*b*), after the fusion of the tail and shoulder cavities, the first rupture occurs following the tail cavity necking. At the rupture position, flow separation occurs. One part continues to move in the direction of the incoming flow, while the other part moves towards the vehicle's bottom wall along the re-entrant flow, forming stagnation high-pressure point I. Eventually, the re-entrant flow impacts the vehicle's bottom wall, forming stagnation high-pressure point III. In the subsequent cavity evolution, the tail

https://doi.org/10.1017/jfm.2025.10422 Published online by Cambridge University Press

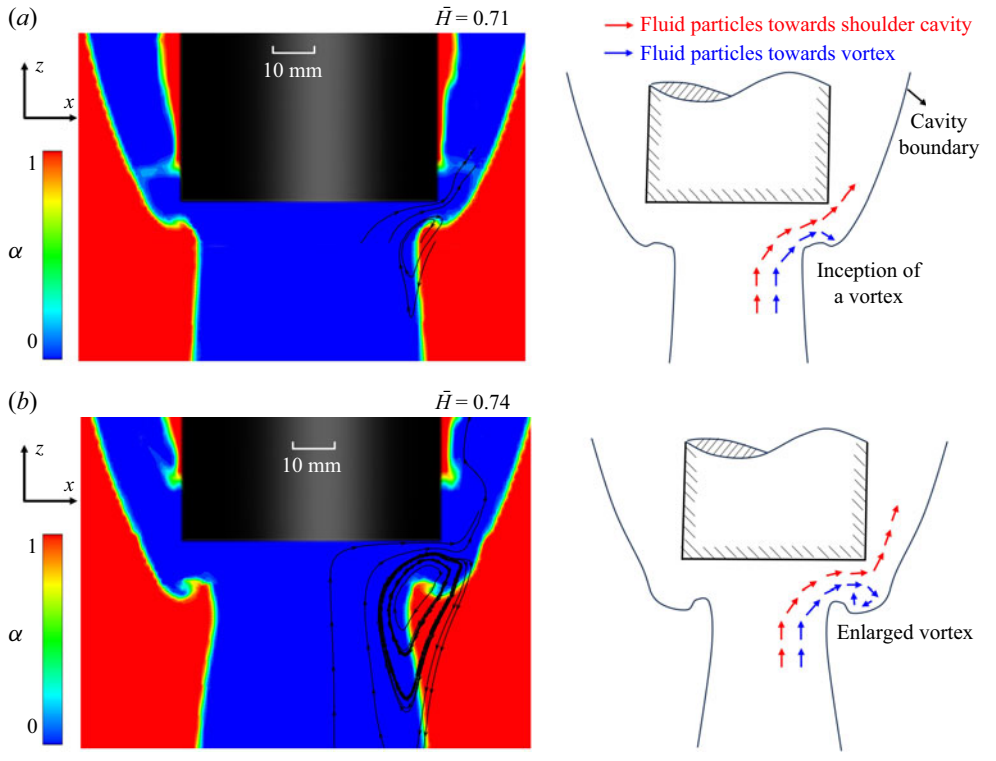


Figure 16. The process of the tail cavity being cut off by the shoulder cavity in case 2. The left-hand side shows the contour of water phase. The right-hand side is a schematic illustration, with red and blue lines indicating the two directions of fluid particles motion within the tail cavity.

cavity is completely cut off by the shoulder cavity, and the vehicle is enveloped by the supercavity at $\bar{H} = 0.89$. At the position of the second rupture, stagnation high-pressure point III forms. As shown in figures 17(*a*) and 17(*c*), on the one hand, point III drives the fluid to accelerate upstream; on the other hand, it decelerates the fluid driven by point I. As the vehicle continues to move, the influence of point I gradually decreases, and the re-entrant flow is driven primarily by point II.

It is evident that stagnation high pressure plays a crucial role in the flow field in the rear region of the supercavity. Therefore, from this perspective, we aim to explain the reasons behind the changes in the variation mode of pressure at the vehicle's bottom wall, after accounting for the shoulder cavity (as discussed about figure 11). The definition of the relative pressure P_{ref} is

$$P_{ref} = \frac{P_{II} - P_{III}}{p_0 + \rho g h_0}, \tag{4.3}$$

where P_{II} and P_{III} represent pressure at stagnation high-pressure points II and III, respectively. As the vehicle continuously moves in the vertical direction, the distance from point I will increase, and its influence will gradually diminish until it disappears. Therefore, only points II and III are considered. Figure 18 shows the variations of $\bar{P}_B$ and P_{ref} with $\bar{H}$, where $\bar{P}_B$ and P_{ref} vary at nearly the same frequency. As discussed in figure 17, the relative pressure between two stagnation high-pressure points influences the velocity of re-entrant flow, which contributes to the change in the variation mode

https://doi.org/10.1017/jfm.2025.10422 Published online by Cambridge University Press

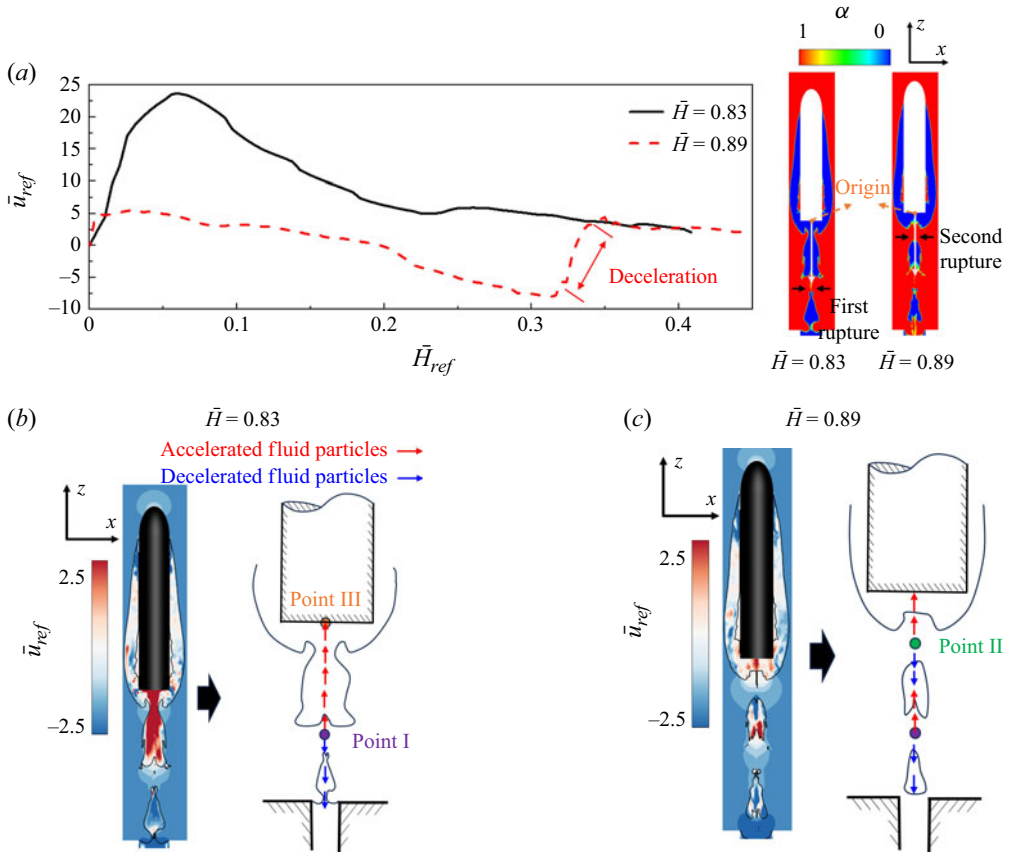


Figure 17. (*a*) The variation of $\bar{u}_{ref}$ with $\bar{H}_{ref}$ in the vehicle's wake region. The right-hand side shows the cavity shape at the corresponding position, with the range of $\bar{u}_{ref}$. (*b*) The contour of $\bar{u}_{ref}$, with diagram at $H = 0.83$. (*c*) The contour of $\bar{u}_{ref}$, with diagram at $H = 0.89$.

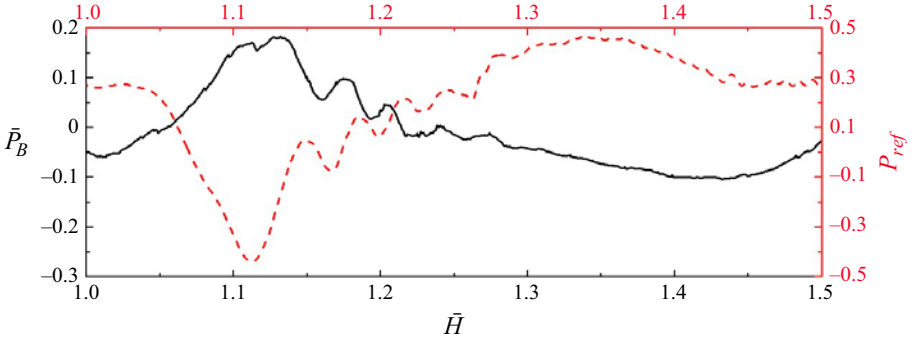


Figure 18. Depth variation laws of pressure under the comparison of $\bar{P}_B$ and P_{ref}.

of $\bar{P}_B$. Thus after the fusion of the shoulder and tail cavities, the driving mechanism of the pressure pulsation at the vehicle's bottom wall transitions from the tail cavity pulsation to the re-entrant flow.

https://doi.org/10.1017/jfm.2025.10422 Published online by Cambridge University Press

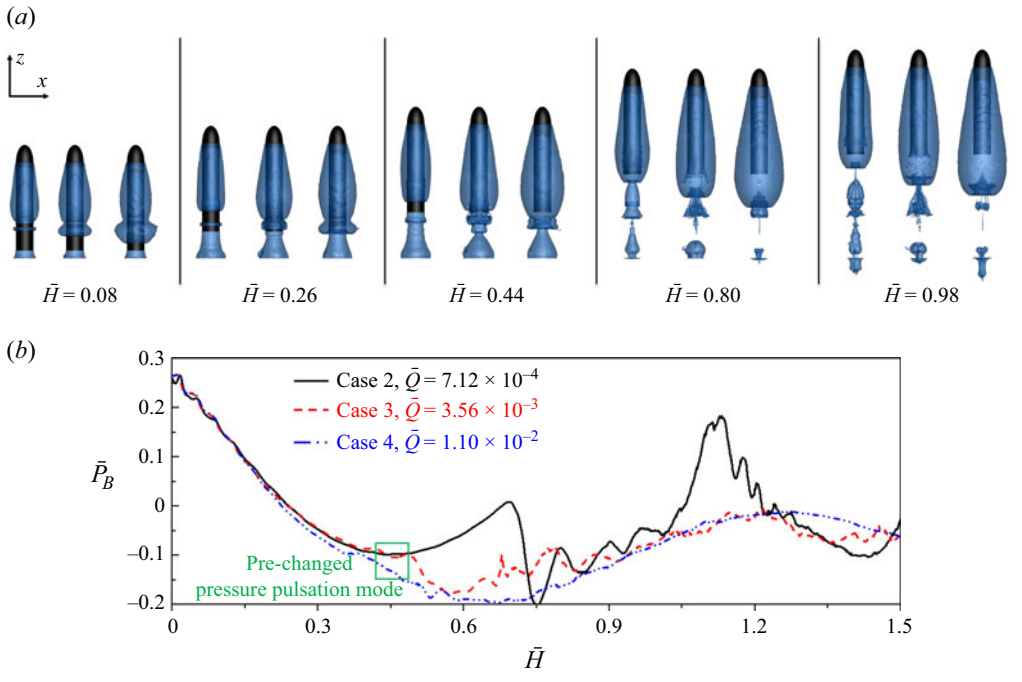


Figure 19. The impact of $\bar{Q}$ on the interaction between the tail and shoulder cavities. (*a*) The flow patterns of cavities in different cases. The flow patterns at each position, from left to right, correspond to cases 2, 3 and 4, respectively. The iso-surface of 90 % water volume fraction is used to illustrate the tail cavity shape. (*b*) The variation of $\bar{P}_B$ with $\bar{H}$.

5. Interaction between shoulder and tail cavities with different ventilation flow rates

In this section, we analyse the impact of shoulder ventilation rates on the interaction between the shoulder and tail cavities. As shown in figure 19(*a*), increasing $\bar{Q}$ leads to progressive expansion in the radial dimension of the shoulder cavity, and accelerates its downstream propagation. At $\bar{H} = 0.08$, the shoulder cavity of case 4 nearly contacts the tail cavity. In the range $\bar{H} = 0.26{-}0.98$, the tail cavity in case 2 undergoes two ruptures: the first induced by necking instability, and the second driven by its interaction with the shoulder cavity. However, in cases 3 and 4, due to the accelerated axial propagation of the shoulder cavity, the tail cavity is prematurely cut off by the shoulder cavity before experiencing the first rupture. This bypasses the necking-induced rupture and leads directly to the second rupture caused by cavity interaction. As a result, an earlier transition in the variation mode of $\bar{P}_B$ is observed in cases 3 and 4, as shown in figure 19(*b*). In addition, as $\bar{Q}$ increases, both the pulsation frequency and amplitude of $\bar{P}_B$ gradually decrease, thereby enhancing structural stability and improving the probability of successful launches. To analyse the fluid mechanism underlying the influence of $\bar{Q}$, a comparative analysis is conducted between cases 2 and 4.

As shown in figure 20(*a*), the vehicle has just exited the launcher tube at $\bar{H} = 0.08$. The internal pressure of the tail cavity significantly exceeds the ambient pressure, generating upstream-propagating pressure that influences the vehicle's lateral wall. As $\bar{Q}$ increases, the shoulder cavity develops earlier towards the vehicle's bottom wall, as shown in figure 20(*b*). The significant pressure gradient between the low-pressure shoulder cavity and the high-pressure tail cavity obstructs further downstream propagation of the

https://doi.org/10.1017/jfm.2025.10422 Published online by Cambridge University Press

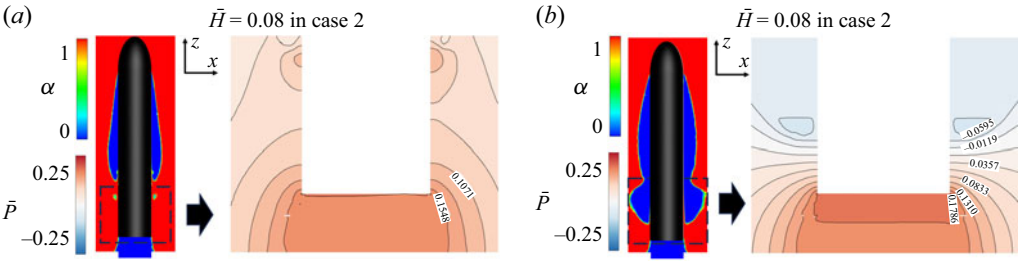


Figure 20. Comparison of the effect of $\bar{Q}$ on $\bar{P}$ between case 2 and case 4. The iso-line of $\bar{P}$ is plotted in the contour of $\bar{P}$ to illustrate the pressure gradient.

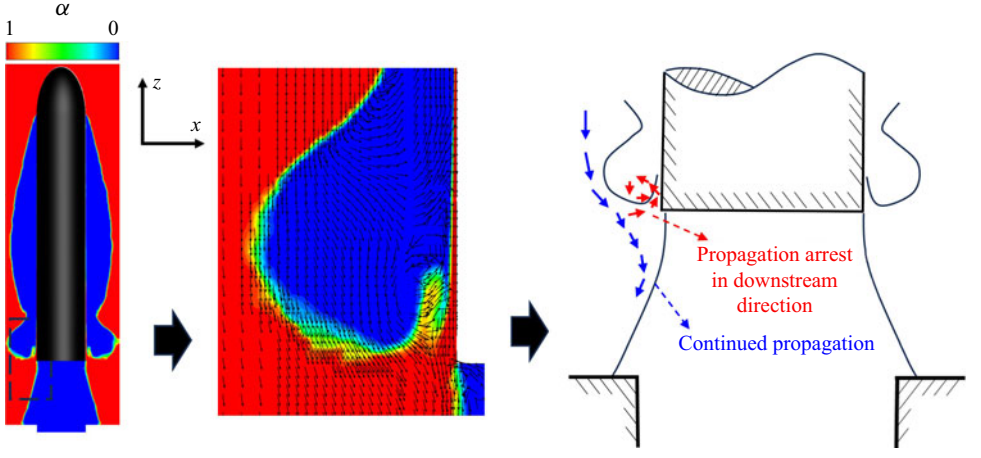


Figure 21. Obstruction induced by the tail cavity to shoulder cavity propagation at $\bar{H} = 0.22$ in case 4.

shoulder cavity. As shown in figure 21, the obstructed shoulder cavity induces a vortex along the inner interface. Without the influence of the vortex, the outer side of the shoulder cavity continues to develop downstream under the action of incoming flow. As the outer side of the shoulder cavity continues to propagate downstream, it eventually covers the tail cavity, as shown in figure 22. This macroscopic flow pattern demonstrates the complete fusion between the tail and shoulder cavities. Under the action of the shoulder cavity, the second rupture of the tail cavity occurs in advance, without the first rupture. It can be concluded that the increased $\bar{Q}$ alters the fusion mode between shoulder and tail cavities, transitioning from the progressive fusion (as discussed in figure 16) to the coverage fusion.

As shown in figure 23, after the fusion of the tail and shoulder cavities, the supercavity is formed. Under low $\bar{Q}$ conditions (case 2), distinct flow separation develops at the end of the cavity, generating high stagnation pressure. This also leads to the high-frequency fluctuation of the pressure on the bottom wall of the vehicle. However, as shown in figure 23(*b*), the increasing $\bar{Q}$ leads to a progressive expansion of the cavity size, resulting in attenuated flow separation. Case 4 exhibits substantially lower stagnation pressure compared to case 2. This results in a reduction in pressure pulsation frequency for case 4, as discussed in figure 19.

6. Conclusion

This study numerically investigates the interaction between shoulder and tail cavities under vertical launching conditions. Detached-eddy simulations are applied for turbulence

https://doi.org/10.1017/jfm.2025.10422 Published online by Cambridge University Press

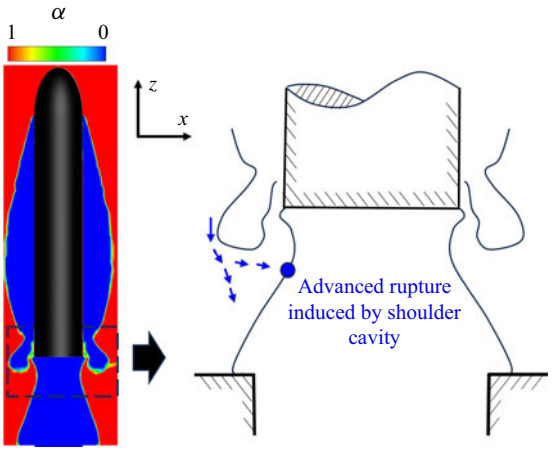


Figure 22. The tail cavity is covered by the shoulder cavity at $\bar{H} = 0.31$ in case 4.

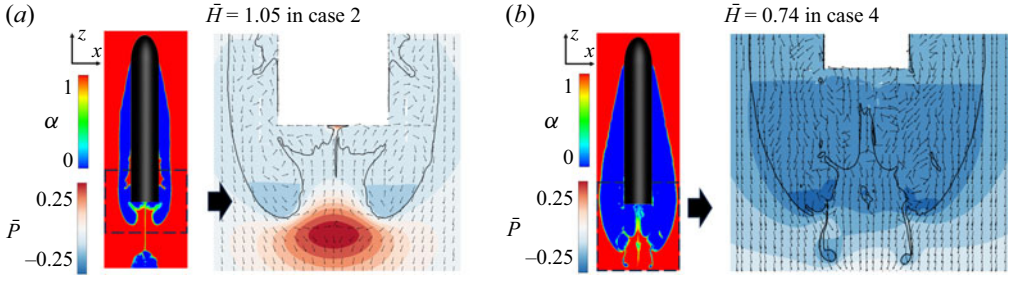


Figure 23. Comparison of the effect of $\bar{Q}$ on the stagnation pressure between case 2 and case 4.

modelling. Adaptive mesh refinement technology is applied to refine the grid near the gas–liquid interface, thereby improving the accuracy in capturing unsteady phenomena such as cavity shedding. A zero-gap overlapping grid technology is utilised to ensure the successful exit of the vehicle from the launcher tube.

The pulsation behaviour of the tail cavity, without the influence of the shoulder cavity, is discussed first. It is found that expansion and contraction coexist within the tail cavity, indicating that changes in cavity volume are relative. When the rate of expansion exceeds that of contraction, the cavity volume increases; conversely, the cavity volume decreases. During the underwater navigation phase, the cavity exhibits a cyclic pulsation process consisting of expansion, over-expansion, contraction and over-contraction.

Consequently, the effect of the ventilated shoulder cavity is taken into consideration. It is found that before the shoulder cavity reaches the tail cavity, its primary influence on the tail cavity arises from the shedding cavities. Driven by the incoming flow, these shedding cavities interact with the tail cavity, disturbing its expansion and contraction rates, thereby inducing instability at the gas–liquid interface. Moreover, the bottom and lateral walls of the underwater vehicle prevent the tail cavity from diffusing to the sidewall of the vehicle, which is defined as wall confinement. Once the shoulder cavity extends to the tail cavity's location, flow separation at its rear further disrupts the tail cavity flow. This disturbance allows the tail cavity to overcome wall confinement, promoting its lateral development along the vehicle's sidewall, and ultimately leading to the fusion of the shoulder and tail cavities. During the fusion process, the tail cavity undergoes two ruptures: the first induced

https://doi.org/10.1017/jfm.2025.10422 Published online by Cambridge University Press

Generation strategies	Mesh size before AMR	Initial grid quantity	Mesh size after AMR	Grid quantity at $\bar{H} = 1.5$
Mesh 1	2.000 mm	4 740 000	0.500 mm	8 580 000
Mesh 2	1.500 mm	7 060 000	0.375 mm	19 200 000
Mesh 3	1.000 mm	15 030 000	0.250 mm	84 390 000

Table 2. Parameters of different grid generation strategies.

by necking instability, and the second driven by its interaction with the shoulder cavity. After the fusion, the pressure driving mode at the vehicle's bottom wall shifts from the tail cavity pulsation to the re-entrant flow. Eventually, the underwater vehicle becomes enveloped by a supercavity and continues to move towards the free surface.

Finally, we investigate the impact of the shoulder ventilation rate on the interaction between the shoulder and tail cavities. Increasing the ventilation rate leads to progressive expansion in the radial dimension of the shoulder cavity and accelerates its downstream propagation. This bypasses the necking-induced rupture, and leads directly to the second rupture, caused by cavity interaction. The fusion mode between shoulder and tail cavities transitions from progressive fusion to coverage fusion. In addition, as the ventilation rate increases, both the pulsation frequency and amplitude of pressure at the vehicle's bottom wall gradually decrease.

Supplementary movie. Supplementary movie is available at https://doi.org/10.1017/jfm.2025.10422.

Funding. The authors would like to acknowledge support from National Natural Science Foundation of China (grant no.U2441206).

Declaration of interests. The authors report no conflict of interest.

Data availability statement. Source data that support the findings of this study are openly available. The experimental data used to generate figure 26 can be found in the online supplementary materials. All other data that support the plots within this paper and other findings of this study are available from the corresponding author upon reasonable request.

Appendix A. Model validation and grid independence validation

Since this numerical simulation accounts for both the shoulder cavity and the tail cavity, validation of numerical methods for both cavities is required.

We established a vertically constrained underwater launching platform for the ventilated shoulder cavity. Figure 24(*a*) exhibits the motion and information collection systems of the platform. A motor is used to tow the underwater vehicle along the slide, allowing it to perform single-degree-of-freedom vertical motion. The vacuum pump is used to reduce atmospheric pressure (P_{atm}) for the scaled-down experiment. The high-speed camera is placed in front of the observation window to collect the information of the ventilated cavity shape. Moreover, as shown in figure 24(*b*), gas is delivered to the air seam through a pipeline. The ventilation system consists of an air compressor for gas supply, and a gas control box for ventilation rate regulation. Experimental and numerical simulation conditions are identical: $Q = 2.8 \times 10^{-4}$, $P_{atm} = 6000$ Pa. The velocity of the underwater vehicle (u_v) in experiment and numerical simulation is shown in figure 25. From $T = 0$ to 0.1 s, the underwater vehicle experiences uniform acceleration, after which it maintains a constant velocity 4.1 m s^{-1}. A comparison of experimental and simulated ventilated cavity shapes is presented in figure 26. At $T = 0.01-0.02$ s, the velocity of

https://doi.org/10.1017/jfm.2025.10422 Published online by Cambridge University Press

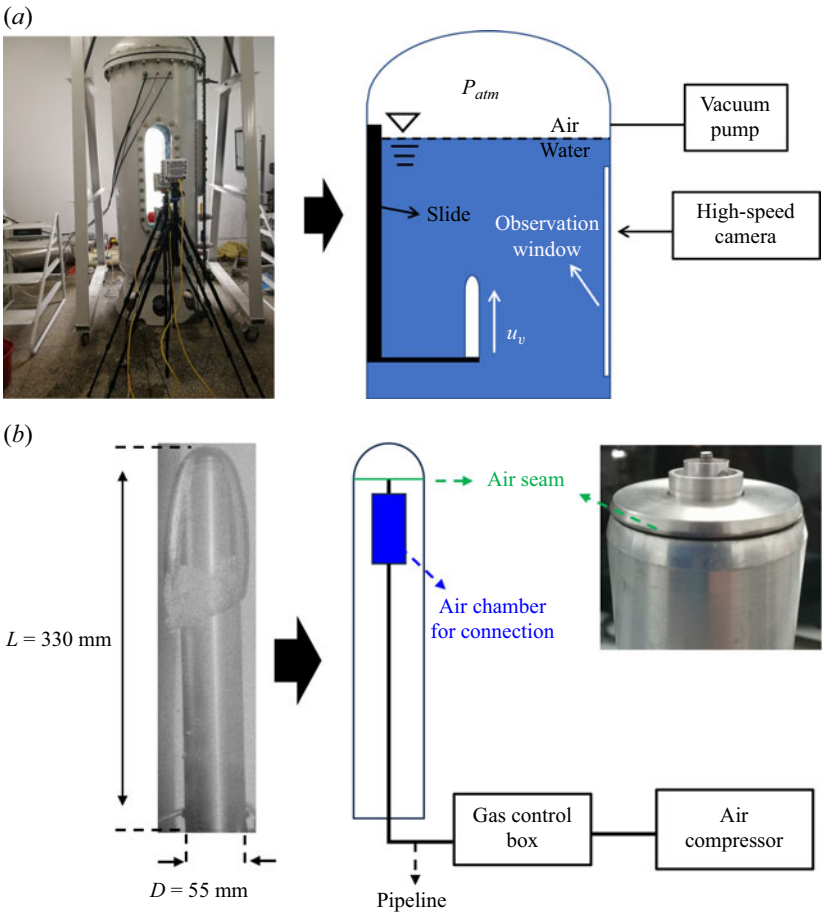


Figure 24. Experimental platform for ventilated cavity. (*a*) Motion system and information collection system. (*b*) Ventilation system.

the vehicle is low. After the discharge of non-condensable gas, a ventilated cavity with a large radial size is formed due to the combined effects of the gas's initial momentum and buoyancy. At $T = 0.06{-}0.08$ s, the end of the ventilated cavity begins to close and develops downstream. At $T = 0.10{-}0.12$ s, the re-entrant jet induces gas–liquid mixing at the ventilated cavity closure, generating the cloudy cavity. Regarding the overall cavity evolution, the experimental and numerical simulation results show strong agreement in the cavity flow patterns. Notably, the numerical model accurately captures special flow patterns, including the cloudy cavity. These findings indicate its effectiveness in simulating ventilated shoulder cavities.

As for the tail cavity, a comparison is made with the experiment conducted by Cheng *et al.* (2022*b*) at Harbin Institute of Technology HT01 Ventilation Cavity Water Tunnel. As shown in figure 27, a 2 mm diameter nozzle is installed at the bottom of the model, exhausting non-condensable gases at a rate of 30 SLPM. Under the influence of incoming flow with velocity 3 m s^{-1}, a tail cavity is formed. The gas leaks from the end of the tail cavity, forming a twin vortex structure with a long-wavelength ripple. The experimental and numerical results show similar flow patterns. Therefore, it can be concluded that the numerical model can accurately predict the tail cavity.

https://doi.org/10.1017/jfm.2025.10422 Published online by Cambridge University Press

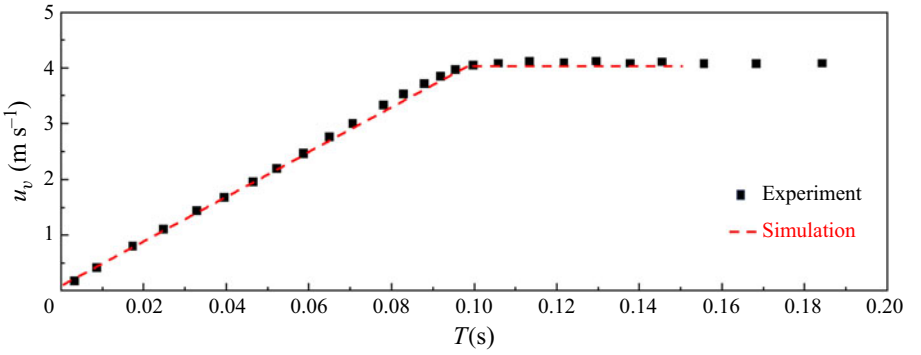


Figure 25. The velocity of the underwater vehicle (u_v) in experiment and numerical simulation.

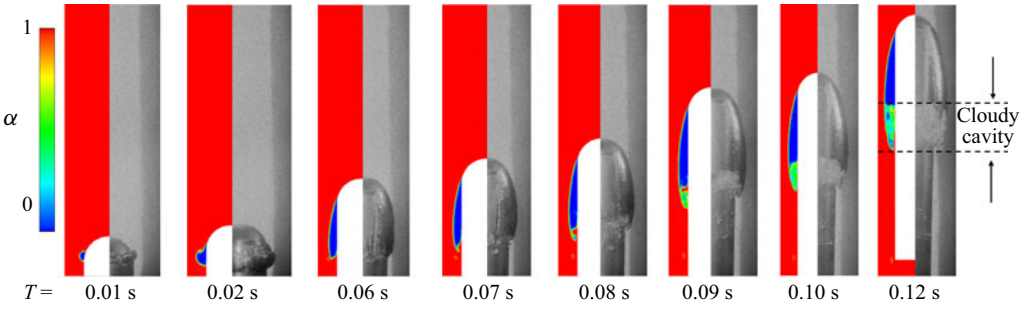


Figure 26. Comparison between the numerical simulation and experimental results of the ventilated shoulder cavity . For more experimental details, please refer to the supplementary material available at https://doi.org/10.1017/jfm.2025.10422.

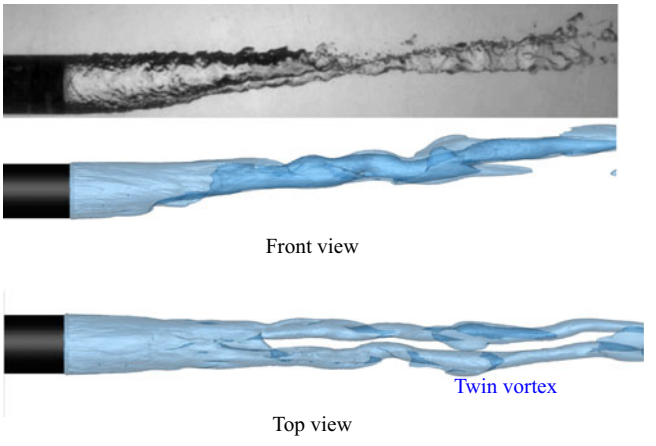


Figure 27. Comparison between the numerical simulation and experimental results of the tail cavity.

Grid independence validation is subsequently carried out, and this study employed three different grid generation strategies: mesh 1, mesh 2 and mesh 3. The grid parameters under different grid strategies are shown in table 2. The variation of $\bar{P}_B$ with $\bar{H}$ in case 2 under different grid generation strategies is shown in figure 28. The results shows that

https://doi.org/10.1017/jfm.2025.10422 Published online by Cambridge University Press

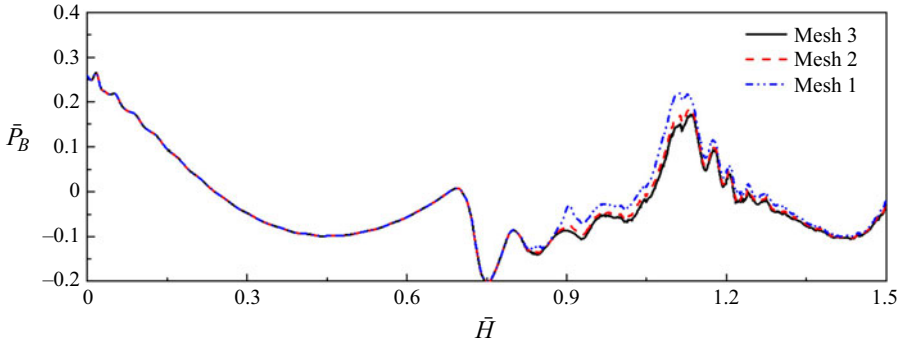


Figure 28. A comparison of cavity shapes under different grid generation strategies.

the variations of $\bar{P}_B$ are quite similar between mesh 2 and mesh 3, while mesh 1 exhibits significant differences. However, the mesh quantity of mesh 3 is huge and requires a lot of computing resources. Therefore, the current numerical simulation uses the meshing strategy of mesh 2.

References

Barbaca, L., Pearce, B.W., Ganesh, H., Ceccio, S.L. & Brandner, P.A. 2019 On the unsteady behaviour of cavity flow over a two-dimensional wall-mounted fence. *J. Fluid Mech.* **874**, 483–525.

Chen, S.R., Shi, Y., Pan, G. & Shan, G. 2021*a* Experimental research on cavitation evolution and movement characteristics of the projectile during vertical launching. *J. Mar. Sci. Engng* **9** (12), 1359.

Chen, Y., Li, J., Gong, Z.X., Chen, X. & Lu, C.J. 2021*b* LES investigation on cavitating flow structures and loads of water-exiting submerged vehicles using a uniform filter of octree-based grids. *Ocean Engng* **225**, 108811.

Chen, X.B., Xiao, W., Gong, R.Y., Yao, X.L. & Hu, S.F. 2022 Experimental investigation of ventilation bubble dynamics around a vertically moving cylinder under reduced ambient pressure. *Fluid Dyn. Res.* **54** (1), 015512.

Cheng, S.H., Quan, X.B., Sha, Y.Y., Yang, Q., Wang, C. & Xu, Y.H. 2022*a* Experimental investigation of the underwater ventilated tail cavity at different angles of attack. *Ocean Engng* **261**, 111916.

Cheng, S.H., Quan, X.B., Zhang, S., Zhang, T.Y. & Li, S. 2022*b* Modeling tail bubble dynamics during the launch of an underwater vehicle using the boundary element method. *J. Hydrodyn.* **34** (3), 434–443.

Epshtein, L. 1973 Characteristics of ventilated cavities and some scale effects. In *Proceedings of the International Symposium IUTAM, Unsteady Water Flow with High Velocities*, pp. 173–185. Nauka.

Fu, G.Q., Zhao, J.L., Sun, L.P. & Lu, Y. 2018 Experimental investigation of the characteristics of an artificial cavity during the water-exit of a slender body. *J. Mar. Sci. Appl.* **17** (4), 578–584.

Gan, N., Liu, Y.Q., Yao, X.L., Chen, Y.Y., Ma, G.H. & Cui, X.W. 2022*a* Experimental investigation on the development features of a gas jet on the surface of a vertical moving body with a constant volume chamber. *Phys. Fluids* **34** (8), 083313.

Gan, N., Yao, X.L., Cheng, S.H., Chen, Y.Y. & Ma, G.H. 2022*b* Experimental investigation on dynamic characteristics of ventilation bubbles on the surface of a vertical moving body. *Ocean Engng* **246**, 110641.

Gan, N., Yao, X.L., Su, B. & Cui, X.W. 2022*c* Study on the dynamic behaviors of a near wall ventilated bubble using OpenFOAM. *Ocean Engng* **257**, 111650.

Gao, S., Shi, Y., Pan, G. & Quan, X. 2022*a* A study on the flow interference characteristics of projectiles successively launched underwater. *Intl J. Multiphase Flow* **151**, 104066.

Gao, S., Shi, Y., Pan, G. & Quan, X.B. 2022*b* A study on the performance of the cavitating flow structure and load characteristics of the vehicle launched underwater. *Phys. Fluids* **34** (12), 125108.

Gao, S., Shi, Y., Pan, G. & Quan, X.B. 2022*c* The transient vortex structure in the wake of an axial-symmetric projectile launched underwater. *Phys. Fluids* **34** (6), 065109.

Gao, S., Shi, Y., Pan, G., Quan, X.B. & Lu, J.W. 2022*d* Study on the wake vortex instability of the projectile launched underwater. *Chin. J. Theor. Appl. Mech.* **54** (9), 2435–2445.

https://doi.org/10.1017/jfm.2025.10422 Published online by Cambridge University Press

GONG, R.Y. 2018 Study on coalescence characteristics of pressure equalizing exhaust bubbles on the surface of underwater vehicles. PhD thesis. Harbin Engineering University.

GUI, Y.Z., CHUANG, Y., WEI, H.P., SUN, T.Z. & YANG, B.Y. 2021 Experimental study on the effects of brash ice on the water-exit dynamics of an underwater vehicle. *Ocean Engng* **117**, 102948.

HIRT, C.W. & NICHOLS, B.D. 1981 Volume of fluid (VOF) method for the dynamics of free boundaries. *J. Comput. Phys.* **39** (1), 201–225.

HU, S.F. 2018 Experiment study on control method of uniformly ventilated cavitation on the surface of high-speed exceeding water vehicle. PhD thesis, Harbin Engineering University.

JIANG, Y.H., SHAO, S.Y. & HONG, J. 2018 Experimental investigation of ventilated supercavitation with gas jet cavitator. *Phys. Fluids* **30** (1), 012103.

KAPANKIN, Y.N. & GUSEV, A.V. 1984 Experimental research of joint influence of fluid and lift power of cavitator on character of flow in cavity rear part and gas departure from it. *Proc. CAHI.* **2244**, 19–28.

KARN, A., ARNDT, R.E.A. & HONG, J. 2016 An experimental investigation into supercavity closure mechanisms. *J. Fluid Mech.* **789**, 259–284.

KAWAKAMI, E. & ARNDT, R.E.A. 2011 Investigation of the behavior of ventilated supercavities. *J. Fluid Engng* **133** (9), 091305.

KIRSCHNER, I.N., MOENY, M.J., KRANE, M.H. & KINZEL, M.P. 2015 Jet-supercavity interaction: insights from physics analysis. *J. Phys. Conf. Ser.* **656** (1), 012156.

KSHATRIYA, S., PATWARDHAN, A. & EAGLESHAM, A. 2007 Experimental studies of ventilated cavities in a channel. *Chem. Engng Sci.* **62** (4), 979–989.

LI, Z.P., SUN, L.Q., XIAO, W. & YAO, X.L. 2019*a* Three-dimensional numerical analysis of near-wall single-orifice ventilated bubble dynamics. *Ocean Engng* **186**, 106066.

LI, Z.P., SUN, L.Q., YAO, X.L. & PIAO, Y. 2019*b* Three-dimensional numerical analysis of horizontal and vertical coalescence of bubbles at two submerged horizontal orifices on the wall. In *Proceedings of the ASME 2019 38th International Conference on Ocean, Offshore and Arctic Engineering*, V002T08A003. American Society of Mechanical Engineers (ASME).

LI, Z.P., SUN, L.Q., YAO, X.L. & WU, G.X. 2020 Numerical investigation of axisymmetric bubble dynamics from a submerged circumferential slit on the cylinder. *Intl J. Multiphase Flow* **125**, 103213.

LIU, H., XIAO, Z.L. & SHEN, L. 2023 Simulation-based study of low-Reynolds-number flow around a ventilated cavity. *J. Fluid Mech.* **966**, A20.

LOGVINOVICH, G.V. 1973 *Hydrodynamics of Free-Boundary Flows*. Halsted Press.

LU, J., BI, D., WANG, C., WEI, Y., WANG, W. & ZHANG, D. 2022*a* Research on the interference characteristics of successively launched underwater projectiles. *Phys. Fluids* **34** (6), 067117.

LU, J.X., WANG, C., SONG, W.C., WEI, Y.J., YU, D.L. & LI, Y.G. 2022*b* Experimental investigation on interference characteristics of projectiles launched successively underwater. *Ocean Engng* **250**, 110824.

MA, G.H., CHEN, F., YU, J.Y. & LIU, H.P. 2018 Flow mechanism and characteristics of pressure-equalizing film along the surface of a moving underwater vehicle. *J. Fluid Engng* **140** (4), 041103.

MA, G.H., CHEN, F., YU, J.Y., WANG, K. & JIANG, S. 2019 Effects of uncertainties in the launch parameters on the pressure-equalizing air film around a vertically launched underwater vehicle. *J. Fluid Engng* **141** (10), 104501.

MA, G.H., ZHANG, W.K., SUN, L.Q., SHI, D.Y., YAO, X.L., YANG, Z.Y. & QU, Z.Y. 2023 Numerical study of flow field similarity problem for high speed water entry of navigating body in different test environments. In *International Conference on Marine Equipment & Technology and Sustainable Development*, pp. 228–246. Lecture Notes in Civil Engineering (LNCE).

MENTER, F.R. 1994 Two-equation eddy-viscosity turbulence models for engineering applications. *AIAA J.* **32** (8), 1598–1605.

NGUYEN, V.T., PHAN, T.H., DUY, T.N. & PARK, W.G. 2022 Unsteady cavitation around submerged and water-exit projectiles under the effect of the free surface: a numerical study. *Ocean Engng* **263**, 112368.

PARYSHEV, E.V. 2006 Approximate mathematical models in high-speed hydrodynamics. *J. Engng Maths* **55** (1–4), 41–64.

QU, Z.Y., YANG, N.N., MA, G.H., YAO, X.L. & CHEN, Y.Y. 2022 Experimental study of unsteady evolution characteristics of ventilated air mass on the cylinder surface. *Ocean Engng* **264**, 112462.

QU, Z.Y., YANG, N.N., MA, G.H., YAO, X.L., ZHANG, W.K., ZHANG, H.T., CHENG, S.H. & QUAN, X.B. 2023 Experimental study on ventilated cavity flow at the tail of underwater vehicle under low surface tension. *Ocean Engng* **267**, 113230.

QUAN, X.B. & CHENG, S.H. 2023 Experimental and numerical investigation on the gas leakage regime for ventilated tail cavity of an underwater vehicle. *J. Hydrodyn.* **35** (1), 46–60.

REN, Z.Y., SUN, L.Q., LI, Z.P. & WEI, X. 2021 Experimental study on the cavitation development and collapse characteristics of underwater vehicle. *Astronaut. Syst. Engng Technol.* **5**, 42–49.

https://doi.org/10.1017/jfm.2025.10422 Published online by Cambridge University Press

REN, Z., WANG, X., CHENG, S., QUAN, X. & YU, Z. 2024 Numerical study on the pulsation characteristics of tail cavities under vertical launching conditions. *Ocean Engng* **305**, 117948.

REN, Z.Y., WANG, X.G., QUAN, X.B. & CHENG, S.H. 2023 Investigation on the impact of underwater vehicle head shapes on the flow and pressure characteristics of ventilated cavity under vertical emission conditions. *Chin. J. Theor. Appl. Mech.* **55** (11), 2518–2530.

REN, Z.Y., WANG, X.G., QUAN, X.B., CHENG, S.H., CHENG, S.N. & CHENG, D.X. 2025 Air mass necking characteristics under vertical launching conditions. *Phys. Fluids* **37** (4), 043351.

SEMENENKO, V.N. 2001 *Artificial Supercavitation. Physics and Calculation*. Ukrainian Academy of Sciences, Kiev Institute of Hydromechanics.

SHAO, S.Y., WU, Y., HAYNES, J., ARNDT, R.E.A. & HONG, J. 2018 Investigation into the behaviors of ventilated supercavities in unsteady flow. *Phys. Fluids* **30** (5), 052102.

SHI, Y., GAO, S., PAN, G. & QUAN, X.B. 2022*a* Simulation of the wake vortex and trajectory characteristics of successively launched multiple projectiles. *Ocean Engng* **249**, 110962.

SHI, Y., REN, J., GAO, S. & PAN, G. 2022*b* Numerical investigation on air film fusion of pressure-equalizing exhaust around shoulder ventilation of submarine-launched vehicle. *J. Mar. Sci. Engng* **10**, 794–818.

SHI, Y., REN, M.-Y., GAO, S., PAN, G. & QUAN, X.-B. 2022*c* A study on the wake vortex encounter and movement interference characteristics of projectiles successively launched underwater. *Acta Armamentarii* **151**, 104066.

SHUR, M.L., SPALART, P.R., STRELETS, M.K. & TRAVIN, A.K. 2008 A hybrid RANS–LES approach with delayed-DES and wall-modelled LES capabilities. *Intl J. Heat Fluid Flow* **29** (6), 1638–1649.

SKIDMOR, G. 2013 The pulsation of ventilated supercavities. PhD thesis, Department of Aerospace Engineering, Pennsylvania State University.

SPALART, P.R., DECK, S., SHUR, M.L., SQUIRES, K.D., STRELETS, M.K. & TRAVIN, A. 2006 A new version of detached-eddy simulation, resistant to ambiguous grid densities. *Theor. Comput. Fluid Dyn.* **20** (3), 181–195.

SPURK, J.H. 2002 On the gas loss from ventilated supercavities. *Acta Mechanica* **155** (3), 125–135.

SUN, L.Q., SUN, C. & ZHAO, L.J. 2014 System design on small-scale solid of revolution exiting water test of scaled missiles. *Transducer Microsyst. Technol.* **33**, 76–79.

SUN, T.Z., ZHANG, J.Y., WEI, H.P., ZHANG, D. & ZHANG, G.Y. 2022 Experimental investigation of the influence of floating ices constraint on the cavity dynamics of an axisymmetric body during the water exit process. *Ocean Engng* **244**, 110383.

SUN, T.Z., ZHANG, X.S., ZHANG, C.X., JIANG, G.Y., SC, & ZONG, Z. 2019 Numerical modeling and simulation of the shedding mechanism and vortex structures at the development stage of ventilated partial cavitating flows. *Eur. J. Mech. B/Fluids* **76**, 223–232.

WANG, Y.W. & HUANG, C.G. 2018 Research progress on hydrodynamics of high speed vehicles in the underwater launching process. *Adv. Mech.* **48**, 1805.

WANG, Y.W., HUANG, C.G., DU, T.Z., FANG, X. & LIANG, N.G. 2012 Mechanism analysis about cavitation collapse of underwater vehicles in a vertical launching process. *Chin. J. Theor. Appl. Mech.* **44**, 39–48.

WANG, Y.W., HUANG, C.G., FANG, X., WU, X.C. & DU, T.Z. 2016 On the internal collapse phenomenon at the closure of cavitation bubbles in a deceleration process of underwater vertical launching. *Appl. Ocean Res.* **56**, 157–165.

WANG, Z.Y., HUANG, B., ZHANG, M.D., WANG, G.Y. & ZHAO, X.A. 2018 Experimental and numerical investigation of ventilated cavitating flow structures with special emphasis on vortex shedding dynamics. *Intl J. Multiphase Flow* **98**, 79–95.

XIONG, C.W., WANG, S.Z., DONG, Q.Q., WANG, S.P. & ZHANG, A.M. 2024 On the interfacial instabilities of a ventilation cavity induced by gaseous injection into liquid crossflow. *J. Fluid Mech.* **980**, A44.

XU, H., WANG, C., LU, H.Z. & HUANG, W.H. 2018 Experimental study on submerged supersonic gaseous jet induced tail cavity. *Acta Phys. Sin.* **67** (1), 014703.

YANG, Q., WANG, C., WEI, Y.J., WANG, Y.L., ZHANG, D.H. & HU, X.Y. 2022*a* Experimental study on the collapse of tail cavity induced by underwater ventilation. *Phys. Fluids* **34** (11), 112111.

YANG, Q., WANG, Y.L., WEI, Y.J., WANG, C. & CHENG, S.H. 2023 Experimental study on tail cavity structure and pressure characteristics of underwater vehicle with tail jet. *Ocean Engng* **281**, 114843.

YANG, Q., XU, H., WANG, C., WEI, Y., MA, L. & SHA, Y. 2022*b* Experimental investigation on flow structure and pressure characteristics of submerged high-speed gaseous jets under co-flow conditions. *Ocean Engng* **266**, 112726.

YAO, X.L., QU, Z.Y., MA, G.H., YANG, N.N., QUAN, X.B. & CHENG, S.H. 2023 Experimental study on motion characteristics of cavity attached to the tail of underwater vehicle. *J. Mar. Sci. Engng* **11** (7), 1287.

https://doi.org/10.1017/jfm.2025.10422 Published online by Cambridge University Press

YAO, X.L., WANG, W.H., MA, G.H., ZHANG, H.T., CHEN, Y.Y., QU, Z.Y., ZHANG, W.K., LU, J.X. & ZHANG, M. 2024 Experimental research on jet induced tail cavities attached to underwater vehicles considering the influence of tail wings. *Ocean Engng* **295**, 116667.

ZHANG, A.-M., LI, S.-M., CUI, P., LI, S. & LIU, Y.-L. 2023 A unified theory for bubble dynamics. *Phys. Fluids* **35** (3), 033323.

ZHANG, J., LI, Y.H. & JIN, P.S. 2005 2D and 3D time-resolved PIV experiments on flow field around vertical and inclined water-exit body. *J. Ship Mech.* **2**, 9–17.

ZHANG, X.S., XU, H., WANG, C., LU, H.Z. & ZHAO, J. 2017 Experimental study on underwater supersonic gas jets in water flow. *Acta Phys. Sin.* **66** (5), 197–207.

ZHANG, X.Y., LYU, X.J. & FAN, X.D. 2022 Numerical study on the vertical water exit of a cylinder with cavity. *China Ocean Engng* **36** (5), 734–742.

ZHANG, Z.Y. 2018 Experimental and numerical methods for active ventilated cavity flows of underwater vehicles. PhD thesis, Harbin Engineering University.

ZHANG, Z.-Y., YAO, X.-L. & ZHANG, A.-M. 2013 Cavitation shape of the three-dimensional slender at a small attack angle in a steady flow. *Acta Phys. Sin.* **62** (20), 204701.

ZHAO, B., YAO, X.-L., ZHAO, Y.-Y., MA, G.-H., FANG,M., ZHANG, M., SHI, Q.-B. & JI, J.-N. 2024 Tail cavity pressure pulsation characteristics under varying ventilation pressure and duration. *Phys. Fluids* **36** (11), 115138.

ZHAO, C.G., WANG, C., WEI, T.J. & ZHANG, X.S. 2015 An experimental study on characteristics of cavitation and ballistic of axisymmetric slender body underwater movement. *J. Phys.: Conf. Ser.* **656**, 012175.

ZHAO, J.L., SUN, L.Q., ZHANG, Z.Y. & YAO, X.L. 2014 Cavitation collapse load characteristic research in the out-of-water process of vehicle. *J. Harbin Inst. Technol.* **46**, 81–86.

ZHAO, X.Y., XIANG, M., ZHANG, W.H., LIU, B. & LI, S.Z. 2021 Numerical study on the stability and closure position of ventailated cavity with a supersonic tail jet. *Chin. J. Theor. Appl. Mech.* **53** (12), 3298–3309.

ZHOU, L.L. & YU, Y.G. 2017 Study on interaction characteristics between multi gas jets and water during the underwater launching process. *Expl Therm. Fluid Sci.* **83**, 200–206.

https://doi.org/10.1017/jfm.2025.10422 Published online by Cambridge University Press